



1 Subseasonal and spatial variability of biomass burning aerosol 2 radiative properties observed over the Southeast Atlantic during 3 ORACLES 2016-2018

4 Logan T. Mitchell¹, Connor J. Flynn¹, Kristina Pistone^{2,3}, Samuel E. LeBlanc^{2,3}, K. Sebastian Schmidt⁴,
5 Hong Chen⁴, Paquita Zuidema⁵, Robert Wood⁶, Jens Redemann¹

6 ¹School of Meteorology, University of Oklahoma, Norman, OK 73072, USA

7 ²Bay Area Environmental Research Institute, Moffett Field, CA 94035, USA

8 ³NASA Ames Research Center, Moffett Field, CA 94035, USA

9 ⁴Laboratory for Atmospheric and Space Physics, University of Colorado, Boulder, CO 80303, USA

10 ⁵Department of Atmospheric Sciences, University of Miami, Miami, FL 33149, USA

11 ⁶Department of Atmospheric Sciences, University of Washington, Seattle, WA 98195, USA

12 *Correspondence to:* Logan T. Mitchell (log.mitch@ou.edu)

13 **Abstract.** During 2016-2018, NASA conducted the ORACLES (ObseRvations of Aerosols above CLouds and their
14 intEractionS) airborne field campaigns to study aerosol-cloud-radiation interactions with the stratocumulus cloud deck over
15 the Southeast Atlantic. ORACLES employed 4STAR (Spectrometer for Sky-Scanning, Sun-Tracking Atmospheric
16 Research) to measure direct solar irradiances and diffuse sky radiances of free-tropospheric Biomass Burning Aerosols
17 (BBA). Aerosol radiative properties, including Single Scattering Albedo (SSA), Aerosol Optical Depth (AOD), Aerosol
18 Absorption Optical Depth (AAOD), Extinction Ångström Exponent (EAE), Absorption Ångström Exponent (AAE), and
19 complex refractive indices are retrieved via an adapted AERONET inversion code. Changes in SSA indicate increased
20 scattering as the biomass burning season progresses, which we attribute to an aerosol brightening from compositional
21 changes, rather than a change in aerosol type, with an apparent lack of Brown Carbon throughout the season. A collection of
22 31 AERONET (AErosol RObotic NETwork) sun/sky photometer stations have operated in Southern Africa for over thirty
23 years (1995-2025), creating a complete aerosol climatology for the first time, which can be compared with SSA and AOD
24 from ORACLES observations. The spatial distributions of in situ SSA are also investigated by latitude, longitude, and
25 altitude. Westward gradual increases and sharper decreases in SSA are attributed to late-transport aging processes identified
26 by previous studies. These processes start further eastward in October, in conjunction with the southeastward shift in source
27 fires. Collectively, ORACLES 4STAR retrievals and in situ measurements have identified subseasonal and spatial trends in
28 SSA over the Southeast Atlantic that complement the Southern African AERONET climatology.



29 **1 Introduction**

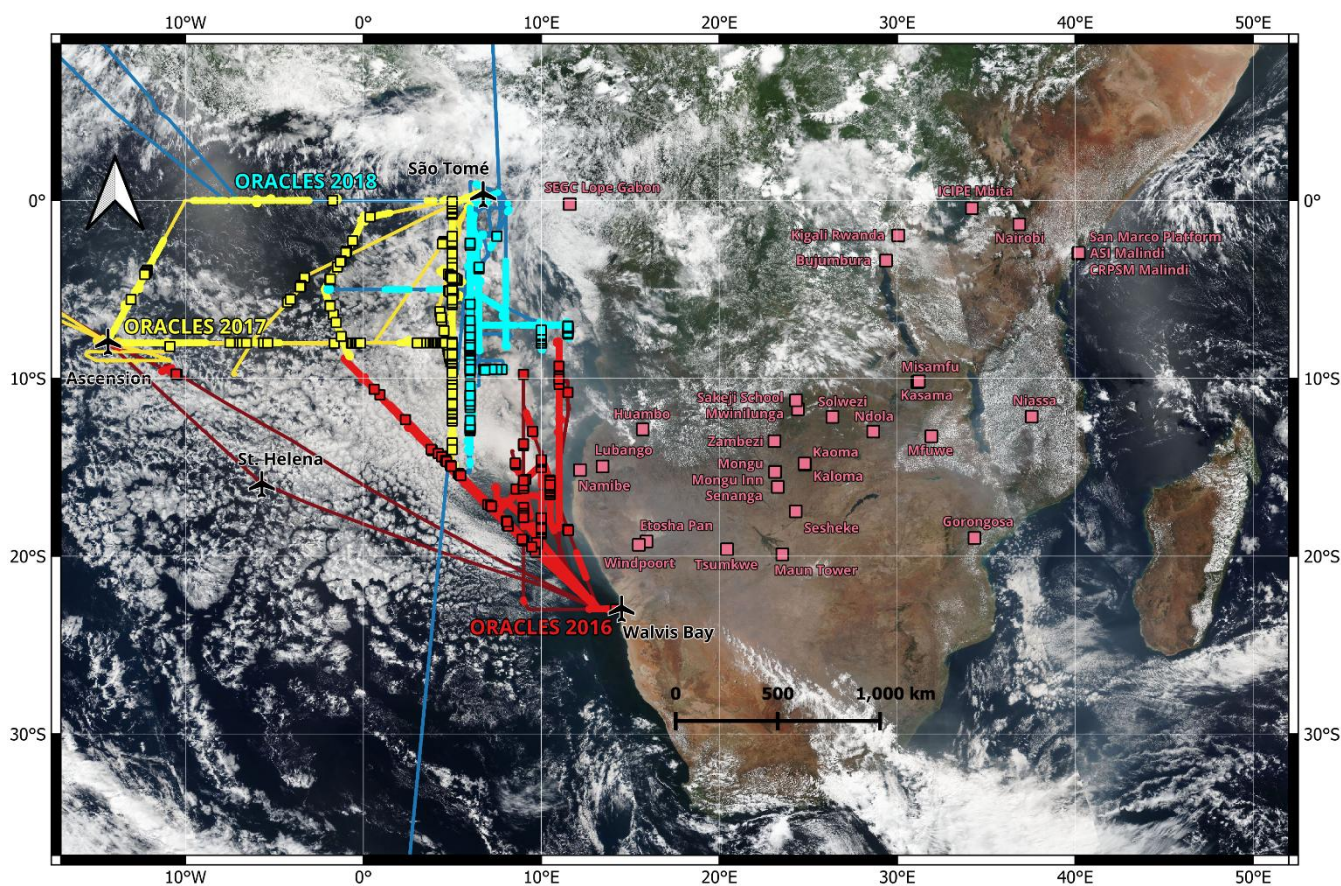
30 The Southeast Atlantic Ocean (SEA) is a region with a high degree of uncertainty regarding aerosol-radiation and
31 aerosol-cloud interactions (Meyer et al., 2013; de Graaf et al., 2014; Mallet et al., 2020; Brown et al., 2021; Che et al., 2021).
32 A major reason for this is the difficulty involved with observing aerosols in the region, especially due to the presence of a
33 semi-permanent subtropical stratocumulus cloud deck (Sakaeda et al., 2011; Waquet et al., 2013). Satellite-based aerosol
34 retrievals, such as those employed by MODIS (MODerate resolution Imaging Spectroradiometer) onboard the Aqua and
35 Terra satellites, are limited by their simplified reflectance-based atmospheric retrieval algorithms when applied to complex
36 atmospheric conditions. In the case of the SEA, aerosol smoke plumes overlie the stratocumulus cloud deck, making it
37 difficult for satellites to discern the above-cloud aerosol properties (Jethva et al., 2024).

38 The remoteness of the SEA also makes it difficult to employ ground-based observations within the region.
39 AERONET (Aerosol RObotic NETwork), a global confederated network of ground-based Cimel sun/sky photometers for
40 the observation of columnar aerosol properties (Holben et al., 1998), is limited to just three stations in the SEA - Ascension
41 Island, St. Helena, and São Tomé. As such, three widely spaced stations yield insufficient resolution to capture most smoke
42 events in the region. As part of the international concerted efforts to study the aerosol-cloud system over the SEA, many
43 AERONET stations within the aerosol source region of Southern Africa were established (Redemann et al., 2021), but the
44 network still has sizeable gaps. The first AERONET station in Southern Africa was established in Mongu, Zambia (15.25 °S,
45 23.15 °E) in 1995, recently allowing for a full thirty-year aerosol climatology of that region for the first time. Thus, airborne
46 campaigns provide a critical link for studying aerosols over the SEA by synergizing with other insights from ground-based
47 measurements and satellite-based observing systems (Zuidema et al., 2016; Zuidema et al., 2018; Formenti et al., 2019;
48 Haywood et al., 2021; Redemann et al., 2021).

49 ORACLES (ObseRvations of Aerosols above CLouds and their intEractionS) was a NASA Earth Venture
50 Suborbital field campaign to study Biomass Burning Aerosols (BBA) over the SEA from 2016 to 2018 (Redemann et al.,
51 2021), using a suite of instruments aboard a P-3 Orion aircraft (2016-2018) and a high-flying ER-2 aircraft (2016 only). One
52 of the instruments deployed on the P-3 aircraft was 4STAR (Spectrometer for Sky-Scanning, Sun-Tracking Atmospheric
53 Research), a sun/sky spectrophotometer for retrieving columnar aerosol radiative properties (Pistone et al., 2019; LeBlanc et
54 al., 2020), serving as an airborne complement to ground-based AERONET retrievals. The campaigns were approximately a
55 month long each and occurred during August 2017, September 2016, and October 2018, collectively covering the peak of
56 Southern Africa's BBA emission season (Queface et al., 2011), which contributes approximately 35 % of global BBA
57 emissions (van der Werf et al., 2010; Granier et al., 2011). In 2016, ORACLES was based out of Walvis Bay, Namibia,
58 while in 2017 and 2018, it was based out of São Tomé (Fig. 1). BBA smoke plumes are transported from mainland Africa to
59 the SEA by the Southern African Easterly Jet (Adebisi and Zuidema, 2016; Holanda et al., 2020), with a maximum jet
60 strength at 3 km in August and 4 km in September and October (Ryoo et al., 2021). Once over the SEA, the BBA overlies



61 and interacts with a semi-permanent subtropical stratocumulus cloud deck (Sakaeda et al., 2011; Wilcox, 2012; Waquet et
 62 al., 2013).



63
 64 **Figure 1:** The ORACLES 2016-2018 P-3 flight paths over the Southeast Atlantic and the 31 AERONET stations in Southern
 65 Africa utilized in this study. ORACLES flight paths are dark lines colored by campaign, with brighter circles for valid in situ
 66 measurements and brighter squares for valid 4STAR sky-scans. Pink squares represent AERONET stations. The ORACLES
 67 headquarters in Walvis Bay, Namibia (2016) and São Tomé (2017-2018), as well as refuelling stations at St. Helena and Ascension
 68 Island are highlighted using airplane symbols. ORACLES 2018 data was transposed 1° eastward as to distinguish it from
 69 ORACLES 2017 data, making the north-south transit leg at 5°E visible for both campaigns. Satellite imagery is true color
 70 corrected reflectance from the VIIRS (Visible Infrared Imaging Radiometer Suite) aboard the NASA/NOAA Suomi satellite for 12
 71 September 2016, courtesy of NASA Worldview.

72
 73 BBA is the largest global source of carbonaceous aerosols (Bowman et al., 2009) and can be composed of strongly
 74 absorbing elemental aerosols called Black Carbon (BC), less-absorbing organic aerosols called Brown Carbon (BrC), and
 75 non-absorbing organic carbon. The full extent of BrC's contribution to both global and regional BBA absorption is the
 76 subject of ongoing research (Andreae and Gelencsér, 2006; Zhang et al., 2020). Previous studies have concluded that little
 77 BrC is present over the SEA (Denjean et al., 2020; Taylor et al., 2020; Wu et al., 2020; Dobracki et al., 2023; Dobracki et al.,
 78 2025), with Taylor et al. (2020) estimating that BrC only accounted for 9 to 11 % of absorption at 405 nm. However, many



79 studies lack optical measurements within the UV spectrum, where BrC absorption is greatest, allowing questions regarding
80 the potential presence of BrC to persist.

81 Absorbing aerosols cause a decrease in environmental albedo that is strongest over brighter surfaces, while non-
82 absorbing aerosols cause an increase in environmental albedo over darker surfaces (Bellouin et al., 2020). Absorbing
83 aerosols generally cause negative radiative forcing (cooling) over the SEA in cloudless conditions but can cause positive
84 radiative forcing (warming) when above a stratocumulus cloud deck (Keil and Haywood, 2003; Chand et al., 2009). BBA
85 interactions with the stratocumulus cloud deck over the SEA are considered a major source of uncertainty for climate
86 modelling of the region (Stier et al., 2013; Zuidema et al., 2016; Haywood et al., 2021; Doherty et al., 2023), in that models
87 show a large spread in predictions and exhibit significant discrepancies relative to observations.

88 The goal of this study is to determine the subseasonal changes in BBA radiative properties that occurred in
89 ORACLES 2016-2018, within the Southern African BBA emission season of August to October. We examine Single
90 Scattering Albedo (SSA) and Aerosol Optical Depth (AOD), the two aerosol properties most pertinent to modellers, but also
91 discuss Aerosol Absorption Optical Depth (AAOD), Extinction Ångström Exponent (EAE), Absorption Ångström Exponent
92 (AAE), and complex refractive indices as well, for a comprehensive view of aerosol radiative changes. SSA from airborne
93 4STAR sky-scans and in situ measurements are compared to assess agreement within the ORACLES 2016-2018 campaigns
94 regarding any apparent subseasonal trends. We also conduct spatial analyses (including latitudinal, longitudinal, and
95 altitudinal) on the in situ SSA data, as to further isolate subseasonal variability from other effects due to chemical and
96 physical processing. The spatial analyses will help to explain apparent discrepancies between datasets, as each ORACLES
97 campaign differs in the latitudes, longitudes, and altitudes sampled. SSA and AOD from ORACLES are also compared
98 against AERONET, allowing for comparison of the BBA radiative properties from the SEA study region and the Southern
99 African source region, as well as a comparison against a full aerosol climatology for the first time.

100 **2 Data and Methods**

101 **2.1 4STAR**

102 4STAR is a sun/sky spectrophotometer measuring direct beam solar irradiances and diffuse sky radiances (Dunagan
103 et al., 2013), designed as an airborne complement to ground-based AERONET Cimel instruments. During ORACLES,
104 4STAR was mounted to the top of the NASA P-3 Orion aircraft, where it observed above-cloud, below-plume columnar
105 aerosol radiative properties (Pistone et al., 2019; LeBlanc et al., 2020). 4STAR also features hyperspectral resolution
106 measurements that permit the retrieval of some gas species (Segal-Rozenhaimer et al., 2014). Direct solar irradiances and
107 diffuse sky radiances measured by 4STAR, along with flight-level albedo calculated from SSFR (Solar Spectral Flux
108 Radiometer) measurements of nadir upwelling and zenith downwelling spectral irradiances (Coddington et al., 2008;
109 Schmidt and Pilewskie, 2012; Cochrane et al., 2019; Cochrane et al., 2021; Schmidt et al., 2021; Cochrane et al., 2022;), are
110 used as inputs in an aerosol inversion code adapted from AERONET version 2.0 (Holben et al., 2006; Dubovik and King,



111 2000; Holben et al., 1998) for airborne use. This code allows us to retrieve aerosol radiative properties from 4STAR and
112 SSFR measurements, including Single Scattering Albedo (SSA), Aerosol Optical Depth (AOD), Aerosol Absorption Optical
113 Depth (AAOD), Extinction Ångström Exponent (EAE), Absorption Ångström Exponent (AAE), Real Refractive Index
114 (RRI), and Imaginary Refractive Index (IRI). SSA, the ratio of aerosol scattering to total aerosol extinction, is one of the
115 most important variables for determining an aerosol's radiative impacts (Takemura et al., 2002; Bergstrom et al., 2007;
116 Moosmüller et al., 2012). The SSA of BBA emitted from Southern Africa can quickly evolve (Abel et al., 2003), requiring
117 highly accurate observations, preferably over the full aerosol life cycle. AOD measures the columnar extinction of light by
118 aerosols, while AAOD measures the columnar absorption of light by aerosols. EAE is the spectral dependence of AOD, with
119 AAE being the spectral dependence of AAOD. The complex refractive indices are one of the primary outputs of the 4STAR
120 retrievals, which are used to iteratively reduce retrieval errors, with the RRI representing aerosol scattering and IRI
121 representing aerosol absorption. 4STAR sky radiance measurements were calibrated in the laboratory using an NIST
122 (National Institute of Standards and Technology) referenceable 12-lamp 36 in. (91.44 cm) integrating sphere (Brown et al.,
123 2005). Whereas 4STAR direct beam measurements were calibrated via refined Langley regressions (Schmid and Wehrli,
124 1995) conducted at Mauna Loa Observatory, before and after deployment (LeBlanc et al., 2020; Mitchell et al., 2025).

125 We utilized 4STAR sky-scans to determine columnar aerosol properties for ORACLES 2016-2018. Our Quality
126 Control (QC) criteria for archival in the NASA ASDC (Atmospheric Science Data Center) repository were:

- 127 (1) AOD (400 nm) > 0.2,
- 128 (2) altitude difference < 50 m,
- 129 (3) mean sky radiance error ($|\text{measured} - \text{fit}|$) < 10 %,
- 130 (4) minimum scattering angle < 6 °,
- 131 (5) maximum scattering angle > 50 °,
- 132 (6) mean scattering angle difference < 3 °,
- 133 (7) maximum scattering angle difference < 10 °,
- 134 (8) covariance matrix sky error < 10 %,
- 135 (9) roll standard deviation < 3 °, and
- 136 (10) passes the retrieval boundary test.

137 Criteria (6) and (7) are only considered over the critical scattering angle range of 3.5 - 30 °. For this study, we
138 additionally required that all sky-scans were below 3 km, as to best ensure a full vertical view of the smoke plume. These
139 sky-scans retrieve at four wavelengths (500, 675, 870, 995 nm), differing slightly from the five-wavelength set (400, 500,
140 675, 870, 995 nm) used by Pistone et al. (2019). We excluded 400 nm due to the presence of an instrument artifact (Mitchell
141 et al., 2025) that affected wavelengths near 420 nm in 2017 and 2018. For uniformity, this was applied to ORACLES 2016
142 as well. These sky-scans are the T0_2016_4wl, R0_2017_4wl, and R0_2018_4wl datasets meeting Selection #2 criteria, as
143 described in Table 2 of Mitchell et al., 2025. The 4STAR sky-scans are summarized in Table 1, along with comparable in
144 situ measurements and ground-based AERONET observations, which are also detailed in the following subsections.



145 **Table 1: The instruments and variables used in this study, along with their reporting wavelengths and valid observation counts.**
 146 **The PSAP & Neph observation counts are for 530 nm, with slightly more measurements at 470 nm, and slightly fewer at 660 nm.**
 147 **The AERONET observation counts are from the 31 Southern African stations displayed in Fig. 1, from 01 July to 31 October, for**
 148 **1995-2025.**
 149

Instrument	Platform	Pertinent Variables	Wavelengths (nm)	Observation Count
4STAR (& SSFR)	ORACLES P-3	SSA, AOD, AAOD, EAE, AAE, RRI, and IRI from sky-scans (using flight-level albedo from SSFR)	500, 675, 870, 995	77 (2016) 141 (2017) 92 (2018)
PSAP & Neph	ORACLES P-3	SSA from in situ PSAP absorption and Neph scattering coefficients	PSAP: 470, 530, 660 Neph: 450, 550, 700	1.1×10^5 (2016) 6.4×10^4 (2017) 7.6×10^4 (2018)
AERONET	Ground	SSA from sky-scans AOD from direct beam measurements	440, 675, 870, 1020	5.0×10^4 (SSA) 5.0×10^5 (AOD)

150 2.2 In Situ Measurements

151 During ORACLES, in situ instruments aboard the P-3 Orion aircraft were operated by the HIGEAR (Hawaii Group
 152 for Environmental Aerosol Research) team. This includes two TSI 3563 nephelometers (Nephs), which determine in situ
 153 aerosol scattering of light. Scattering coefficients are measured at three wavelengths (450, 550, 700 nm) using Anderson and
 154 Ogren (1998) corrections that account for Scattering Ångström Exponent (SAE) and depend upon both wavelength and the
 155 presence/lack of a submicron impactor. Two Radiance Research PSAPs (Particle Soot Absorption Photometers), also
 156 operated by HIGEAR aboard the P-3 aircraft, were used to determine in situ aerosol light absorption. Absorption coefficients
 157 are measured at three wavelengths (470, 530, 660 nm) using Virkkula (2010) wavelength-averaged corrections from the
 158 fittings of transmission correction functions, black aerosol experiments, and ammonium sulfate experiments.

159 A newly processed in situ SSA dataset for ORACLES 2016-2018 was also used in this study. SSA was calculated
 160 from 1 Hz Neph scattering coefficients (σ_{scat}) and PSAP absorption coefficients (σ_{abs}) that had been subjected to a 10 s
 161 rolling average. A scattering coefficient screening of $> 10 \text{ Mm}^{-1}$ was applied per wavelength to reduce statistical noise, such
 162 that SSA_{470} requires $\sigma_{\text{scat}_{470}} > 10 \text{ Mm}^{-1}$, SSA_{530} requires $\sigma_{\text{scat}_{530}} > 10 \text{ Mm}^{-1}$, and SSA_{660} requires $\sigma_{\text{scat}_{660}} > 10 \text{ Mm}^{-1}$.
 163 Additional screenings were also applied to target the free-tropospheric BBA smoke plume (carbon monoxide concentrations
 164 $> 130 \text{ ppbv}$ and altitude $> 1.5 \text{ km}$) allowing for comparison with 4STAR (Mitchell et al., 2026). BBA is the dominant
 165 aerosol present in the free troposphere over the SEA, but it may be mixed with or dominated by sea salt aerosols within the
 166 boundary layer (Dang et al., 2022), warranting the latter's exclusion. Due to the 10 s rolling average, when using the in situ
 167 data for statistical analyses, we assume that the number of independent samples is one tenth of the observation count.

168 The ORACLES campaigns span 09 August to 02 September 2017, 27 August to 27 September 2016, and 24
 169 September to 25 October 2018. For simplicity, we will often summarize the ORACLES 4STAR and in situ data per
 170 campaign, which we will refer to as “months”, as most research flights occurred in August 2017, September 2016, and
 171 October 2018, respectively. For valid 4STAR retrievals, only one research flight was outside of the primary month per
 172 campaign. It is a similar case for valid in situ measurements, except that ORACLES 2018 had two research flights outside of
 173 the primary month.



174 **2.3 AERONET**

175 AERONET cloud-screened (level 1.5) AOD from direct beam measurements and SSA from almucantar and hybrid
176 sky-scans (Giles et al., 2019; Sinyuk et al., 2020) were obtained for 31 Southern African stations (Fig. 1) for 1995-2025 to
177 represent an aerosol climatology of ground-based measurements of similar data quality to 4STAR. The primary purpose of
178 analyzing the climatology is to assess the representativeness of the three-year ORACLES period. This dataset was then
179 limited to 2016-2018, so that just the concurrent ORACLES years could be compared as well, which contains approximately
180 31 % of the data within the full climatology.

181 When selecting AERONET stations, we limited the latitudinal range to 0° - 20° S, targeting only the near-source
182 AERONET stations upwind of the SEA, while aiming to avoid any anticyclonic recirculations that transport BBA back
183 towards the southerly latitudes of mainland Africa (Adebisi and Zuidema, 2016; Redemann et al., 2021). These latitudinal
184 restrictions were not applied to ORACLES 2016 in situ data so that its full latitudinal dependence could be observed, while
185 only one valid 4STAR sky-scan occurred south of 20° S.

186 **3 Results**

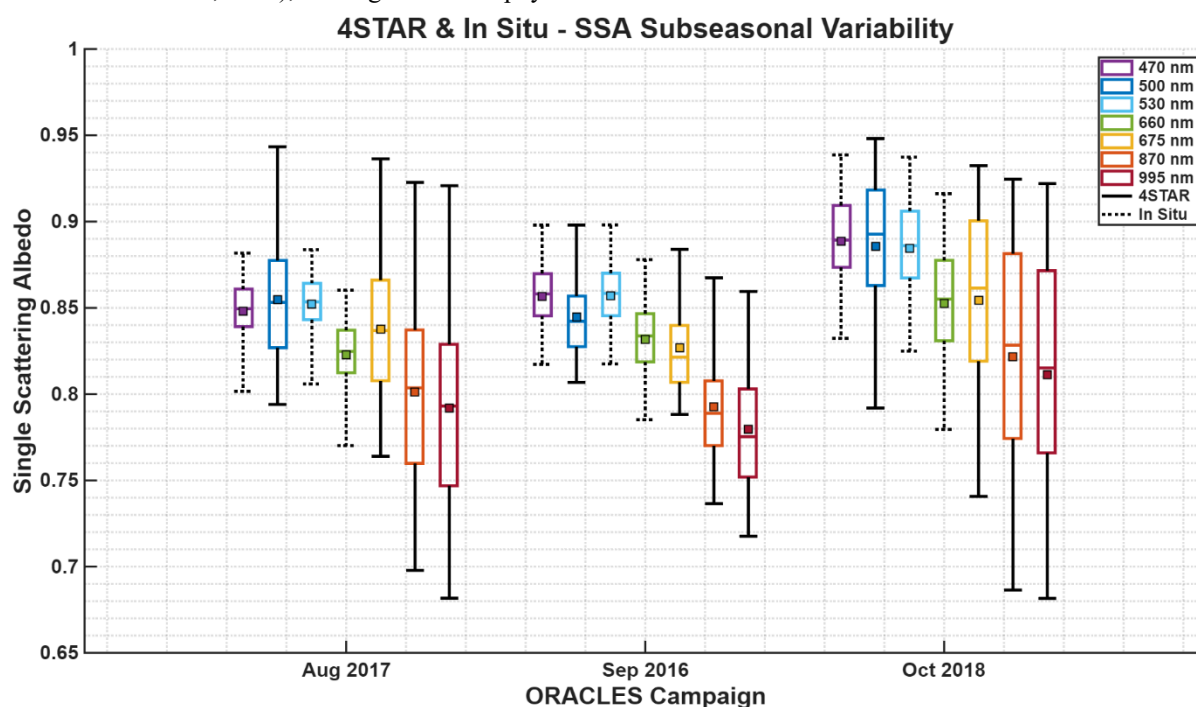
187 **3.1 SSA Subseasonal Analysis**

188 4STAR radiative properties, including SSA, AOD, AAOD, EAE, AAE, and complex refractive indices, are
189 organized by ORACLES campaign month (August 2017, September 2016, October 2018) and box-plotted to illustrate their
190 subseasonal variabilities. All four wavelengths are displayed within each campaign, so that their spectral dependence can
191 also be observed. For SSA, in situ measurements at all three PSAP wavelengths are also included.

192 Both 4STAR retrievals and in situ measurements exhibit an increase in median SSA over the course of the BBA
193 emission season (Fig. 2), with the increase from August to October ranging from +0.02 at longer wavelengths to +0.04 at
194 shorter wavelengths. 4STAR displays a decrease in SSA medians from August to September not found in the in situ data,
195 which we address later using spatial analyses. The 4STAR SSA variability of 0.79-0.95 at 500 nm for ORACLES 2017
196 aligns with that found by Cochrane et al. (2021) using an SSFR absorption-derived method. Applying a two-sample
197 Wilcoxon rank sum test (which determines if the samples are from continuous distributions with equal medians) to the in situ
198 data yields p-values < 0.001 for both monthly transitions (August-September and September-October) at all three PSAP
199 wavelengths, indicating a strongly significant increase through the season. Applying the same test to the 4STAR sky-scans
200 for the transition from August to September yields p-values < 0.05 at 500 and 675 nm, with p-values of 0.17 and 0.07 at 870
201 and 995 nm, while September to October yields p-values < 0.001 at all four 4STAR wavelengths. This indicates that the
202 August to September decrease only recorded by 4STAR is not statistically significant at the longer wavelengths, whereas the
203 September to October increase is strongly significant like that found in the in situ data.



204 This shows an increase in aerosol scattering, relative to total extinction, suggesting aerosol brightening as the
 205 season progresses. An SSA increase of this magnitude has a complex and significant impact on variables related to aerosol-
 206 radiation interactions, including the Direct Aerosol Radiative Effect (DARE) and heating rates, so it needs to be properly
 207 accounted for in aerosol models. An increase in mid-visible median SSA from 0.84 in August to 0.88 in October can cause
 208 critical albedo (the scene albedo whereby an overlying aerosol layer switches from warming to cooling) to increase from
 209 0.23 to 0.27 (Cochrane et al., 2021). The critical albedo’s sensitivity to SSA is particularly important for clear and partially
 210 cloudy conditions with flight-level albedos less than 0.25, with heightened SSA in October decreasing the chances for
 211 aerosol warming. This implies that heightened SSA in October is likely to weaken DARE and reduce heating rate efficiency
 212 aloft (Cochrane et al., 2022), which in turn, would decrease atmospheric stability. This SSA increase has been noted by
 213 previous studies and is likely linked to the southeastward shift in fires (Eck et al., 2013; Redemann et al., 2021; Choi et al.,
 214 2024; Tatro and Zuidema, 2025), although the exact physical cause has been unclear.



215
 216 **Figure 2: Subseasonal variability of 4STAR (solid) and in situ (dashed) SSA from ORACLES 2016-2018. Boxes show the**
 217 **interquartile range, while whiskers extend to the 5th and 95th percentiles. Central lines are medians and squares are means.**

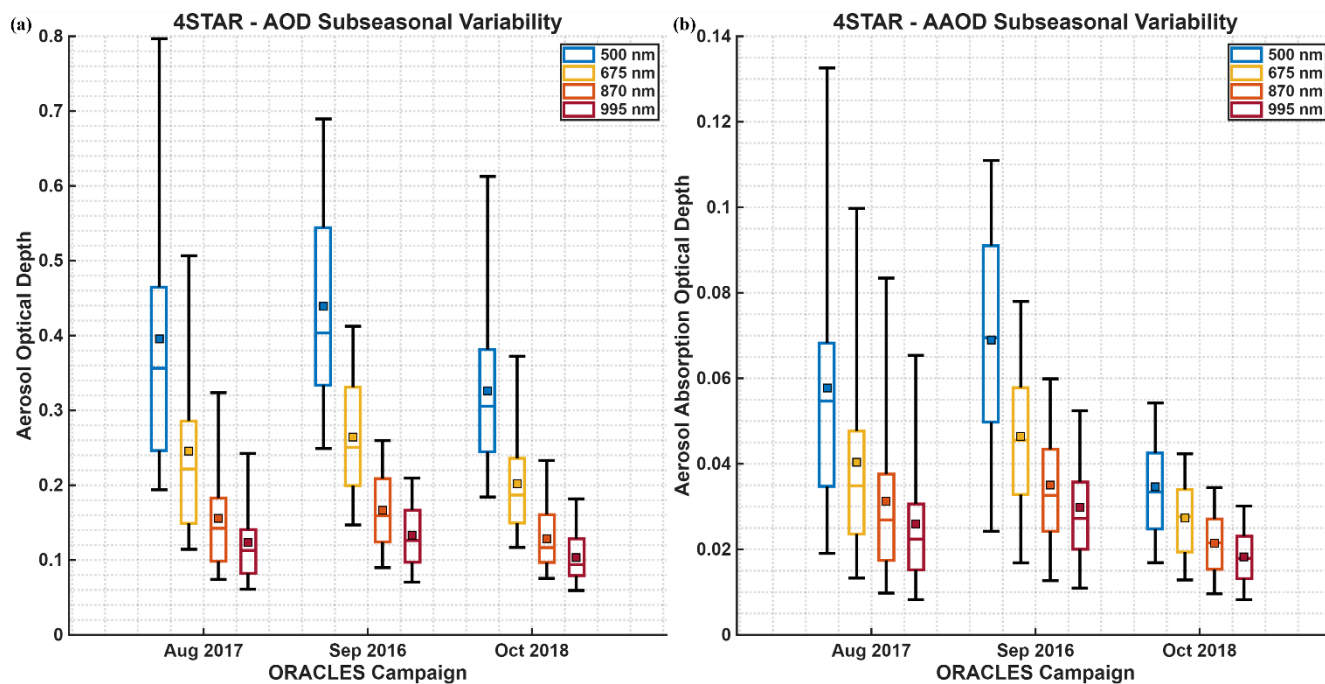
218 3.2 AOD and AAOD Subseasonal Analysis

219 At 500 nm, median AOD (and standard deviations) increases from 0.36 in August to a peak of 0.40 in September,
 220 then decreases to 0.31 in October, with similar relative changes at longer wavelengths (Fig. 3). Applying a two-sample
 221 Wilcoxon rank sum test to AOD, the transition from August to September yields p-values < 0.05, while September to
 222 October yields p-values < 0.001 (both considering all four wavelengths). This indicates that the August to September AOD



223 increase is moderately significant, whereas the September to October decrease is strongly significant. Although burned area
 224 in Southern Africa peaks in August, previous studies have found that persistent aerosol accumulation in the atmosphere
 225 delays the peak in aerosol loading until September (Eck et al., 2013; Adebisi et al., 2015; Redemann et al., 2021; Tatro and
 226 Zuidema, 2025). 4STAR AOD being greatest in September reflects these previous findings, but the transition from August is
 227 less dramatic, likely due to the lack of sampling in early August, when AOD would be lower.

228 AAOD parallels the trend in AOD, with median values at 500 nm of 0.055 in August, 0.069 in September, and
 229 0.033 in October, which is again reflected at longer wavelengths as well. Applying the two-sample Wilcoxon rank sum test
 230 to AAOD, the transition from August to September yields p-values < 0.005 , while September to October yields p-values $<$
 231 0.001 (again considering all four wavelengths). This indicates that the initial AAOD increase is strongly significant, while
 232 the subsequent AAOD decrease has even greater significance. The similarity to the AOD trend is somewhat unsurprising, as
 233 AAOD is also an extensive property and thus dependent upon aerosol loading, but the correlated behavior suggests that there
 234 is not a significant change in aerosol type, which will be further verified using EAE and AAE in the next section. The
 235 decrease in AAOD from September to October is concurrent with the SSA increase from Fig. 2, indicating an absorption
 236 decrease coincident with the aerosol brightening.



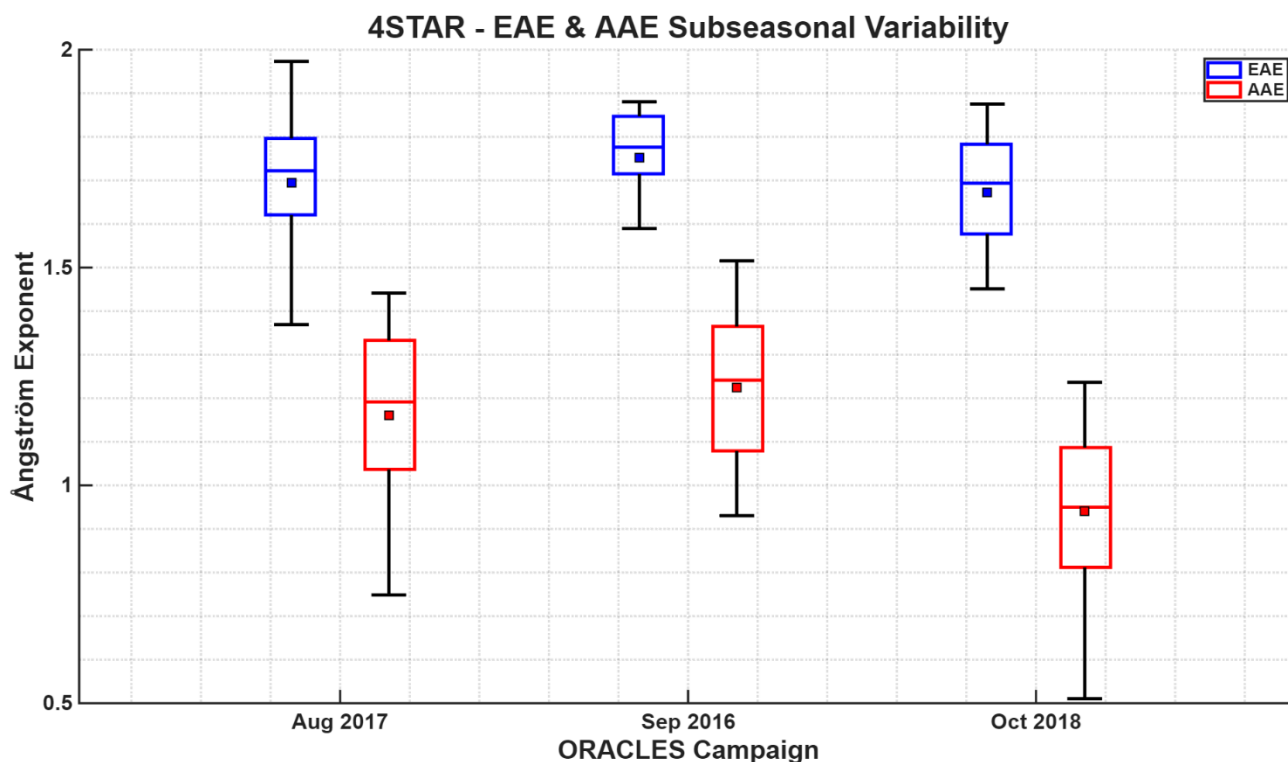
237

238 **Figure 3: Subseasonal variability of 4STAR (a) AOD and (b) AAOD from ORACLES 2016-2018. Boxes show the interquartile**
 239 **range, while whiskers extend to the 5th and 95th percentiles. Central lines are medians and squares are means.**



240 3.3 EAE and AAE Subseasonal Analysis

241 EAE and AAE were calculated by performing log-log spectral linear regressions of AOD and AAOD, respectively,
242 using all four wavelengths (500, 675, 870, 995 nm) as input. The EAE campaign medians are centered near 1.73 (Fig. 4),
243 with about 90 % of the total distribution falling within the 1.5 - 2.0 range, indicating fine aerosols (Schuster et al., 2006).
244 There is greater variability within the AAE distributions, which is expected given its sensitivity to the much smaller
245 absorption component. The AAE interquartile ranges are about 1.05 - 1.35 for August and September, which drops to 0.8 -
246 1.1 in October, suggesting the dominance of BC throughout the season. The presence of BrC cannot be fully discounted, as
247 this study was unable to directly examine the UV wavelengths that are best absorbed by BrC (Alexander et al., 2008), but the
248 lack of BrC contributions does align with previous findings (Denjean et al., 2020; Taylor et al., 2020; Wu et al., 2020;
249 Dobracki et al., 2023; Dobracki et al., 2025). However, if the aerosol brightening in October was caused by increased BrC
250 contributions, we would expect the AAE to increase, rather than decrease (Russell et al., 2010). Since there does not appear
251 to be significant changes in aerosol types during the BBA emission season, such as the processes described by Bond et al.
252 (2013), we conclude that the aerosol brightening is instead due to changes in aerosol composition (Eck et al., 2013). BBA
253 composition is dependent upon both fuel type and burning conditions, with the less-efficient smoldering fire phase
254 generating more organic carbon and less BC than during the flaming phase (Levin et al., 2010; Collier et al., 2016; Jen et al.,
255 2019; Dobracki et al., 2025). Back-trajectories performed by Dobracki et al. (2023) source less-scattering September BBA
256 from grass fuels in the Miombo woodlands of Angola. The source fires shift southeastward in October to Botswana,
257 Zimbabwe, and South-Central Mozambique, in alignment with the higher SSA values observed in that region (Eck et al.,
258 2013; Choi et al., 2024; Tatro and Zuidema, 2025).

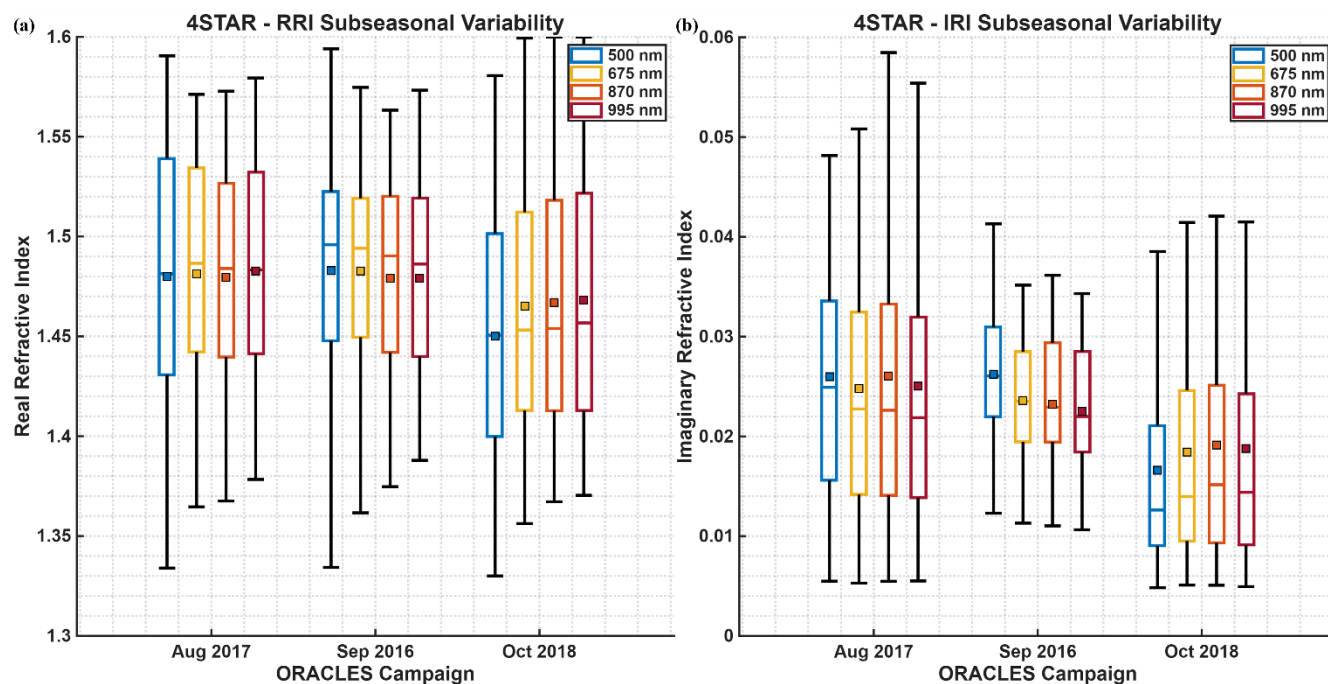


259

260 **Figure 4: Subseasonal variability of 4STAR EAE (blue) and AAE (red) from ORACLES 2016-2018. Boxes show the interquartile**
 261 **range, while whiskers extend to the 5th and 95th percentiles. Central lines are medians and squares are means.**

262 **3.4 Complex Refractive Indices Subseasonal Analysis**

263 We also examined the subseasonal variability of the complex refractive indices (Fig. 5), including both RRI and
 264 IRI. At 500 nm, median RRI increases from about 1.48 in August to 1.50 in September, then falling to 1.45 in October, with
 265 similar relative changes at longer wavelengths. Applying a two-sample Wilcoxon rank sum test to RRI, the transition from
 266 August to September is not statistically significant at any wavelength, while September to October yields p-values < 0.05 at
 267 500 and 675 nm, with p-values of 0.10 and 0.14 at 870 and 995 nm. The IRI trend appears similar, with the IRI median at
 268 500 nm increasing from about 0.025 in August to 0.026 in September, and falling to 0.013 in October, which is again
 269 reflected at the longer wavelengths. Applying the same test to IRI, the transition from August to September is once again not
 270 statistically significant, but the transition from September to October yields p-values < 0.001 (both considering all four
 271 wavelengths). The lack of an increase in RRI coupled with a strong decrease in IRI suggests that the aerosol brightening in
 272 October is dependent upon a decrease in aerosol absorptivity, rather than an actual increase in its scattering.



273

274 **Figure 5: Subseasonal variability of 4STAR (a) RRI and (b) IRI from ORACLES 2016-2018. Boxes show the interquartile range,**
 275 **while whiskers extend to the 5th and 95th percentiles. Central lines are medians and squares are means.**

276 4 Discussion

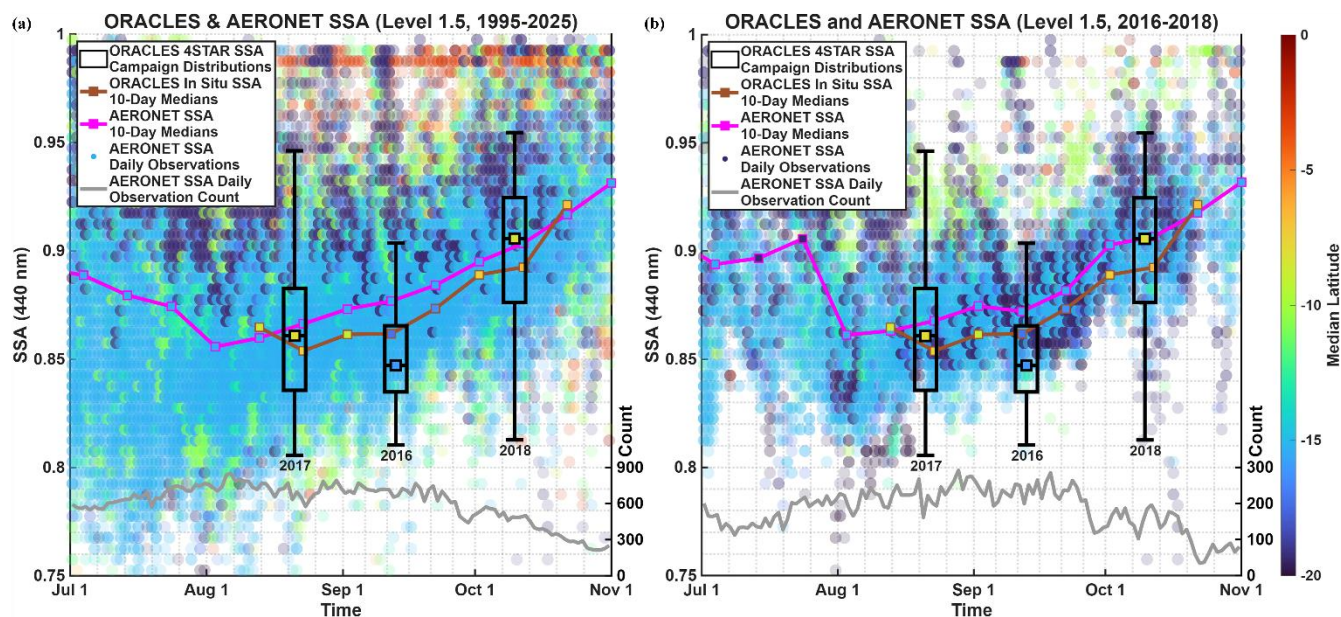
277 4.1 ORACLES and AERONET

278 To compare SSA and AOD from ORACLES and AERONET, we updated and expanded upon Fig. 3 from
 279 Redemann et al. (2021). AERONET observations are discretized into cells of 0.005 SSA (or 0.05 AOD) per day, then
 280 colored by median latitude to emphasize which stations are most contributing to the dataset, with opacity weighted by the
 281 number of observations. 10-day SSA and AOD medians are calculated from the AERONET observations, centered on Julian
 282 dates ending in five. The same method was also applied to determine 10-day medians from ORACLES in situ SSA. SSA and
 283 AOD from 4STAR are box-plotted per campaign due to the limited number of sky-scans, compared to the high volume of
 284 AERONET and in situ observations, centered on the median campaign dates of 21 August 2017, 12 September 2016, and 10
 285 October 2018. Log-log spectral quadratic regressions of 4STAR AOD and AAOD were performed, with derivatives taken at
 286 500 nm, resulting in EAE_{500} and AAE_{500} , like the procedure performed by Redemann et al. (2006). EAE_{500} (and AAE_{500})
 287 were used to extrapolate AOD (and AAOD) from 500 nm to 440 nm, allowing for the calculation of 4STAR SSA at 440 nm.
 288 In situ SSA was extrapolated using a spectral linear regression, requiring defined SSA inputs from all three wavelengths
 289 (470, 530, 660 nm).



290 After extrapolating to 440 nm, 4STAR and in situ median SSA still show a subseasonal increase of about 0.04 (Fig.
291 6), in agreement with the shorter wavelengths from Fig. 2. This is echoed by the Southern African AERONET stations,
292 which also saw an increase in median SSA of about 0.04 from 23 August to 12 October (the closest 10-day medians to the
293 ORACLES 2017 and 2018 campaign medians), for both the three concurrent campaign years of 2016-2018, as well as for
294 the aerosol climatology of 1995-2025. The AERONET and in situ 10-day SSA medians largely agree on the slope of this
295 increase, barring the very start and end of the ORACLES campaign period. There is good agreement between 4STAR and
296 AERONET SSA medians for ORACLES 2017 and 2018, but the September decrease in SSA shown by 4STAR is not
297 reflected in either the AERONET or in situ datasets. We believe that the southerly location of the ORACLES 2016 campaign
298 impacted 4STAR's September SSA distribution, which is explored further by our spatial analyses.

299 The AERONET station at Windpoort, Namibia (19.37 °S, 15.48 °E) is the greatest contributor of July-October SSA
300 retrievals, supplying 18.5 % of 1995-2025 and 25.3 % of 2016-2018 data, with the latter percentage increasing the station's
301 visibility in Fig. 6b. The second greatest contributor of July-October SSA retrievals is the AERONET station at Mongu Inn,
302 Zambia (15.27 °S, 23.13 °E), supplying 18.0 % of 1995-2025 and 18.7 % of 2016-2018 data, and is well-represented within
303 both panels of Fig. 6 due to its centrality within the latitudinal distribution of AERONET observations. The two AERONET
304 time series are in remarkable agreement with one another, highlighting the ability of the ORACLES 2016-2018 campaigns to
305 reflect a much longer data record. The good agreement between ORACLES and AERONET also suggests that the BBA
306 radiative properties over the Southeast Atlantic remain largely reflective of those emitted from Southern Africa, showcasing
307 how data from ORACLES (and other SEA campaigns) can be relevant outside of its direct study region.



308

309 **Figure 6: 4STAR and in situ SSA from ORACLES 2016-2018, with AERONET SSA for (a) 1995-2025 and (b) 2016-2018. Black**
 310 **boxes show 4STAR's interquartile range, with square medians, and whiskers extending to the 5th and 95th percentiles. 10-day**
 311 **medians are shown for in situ (brown) and AERONET (pink). Background data are AERONET observations, with opacity**
 312 **weighted by count. The daily count of AERONET observations (gray) is also displayed at the bottom. All other colors represent**
 313 **the median latitude of the observations used to calculate each median SSA value or fill in each cell.**

314

315

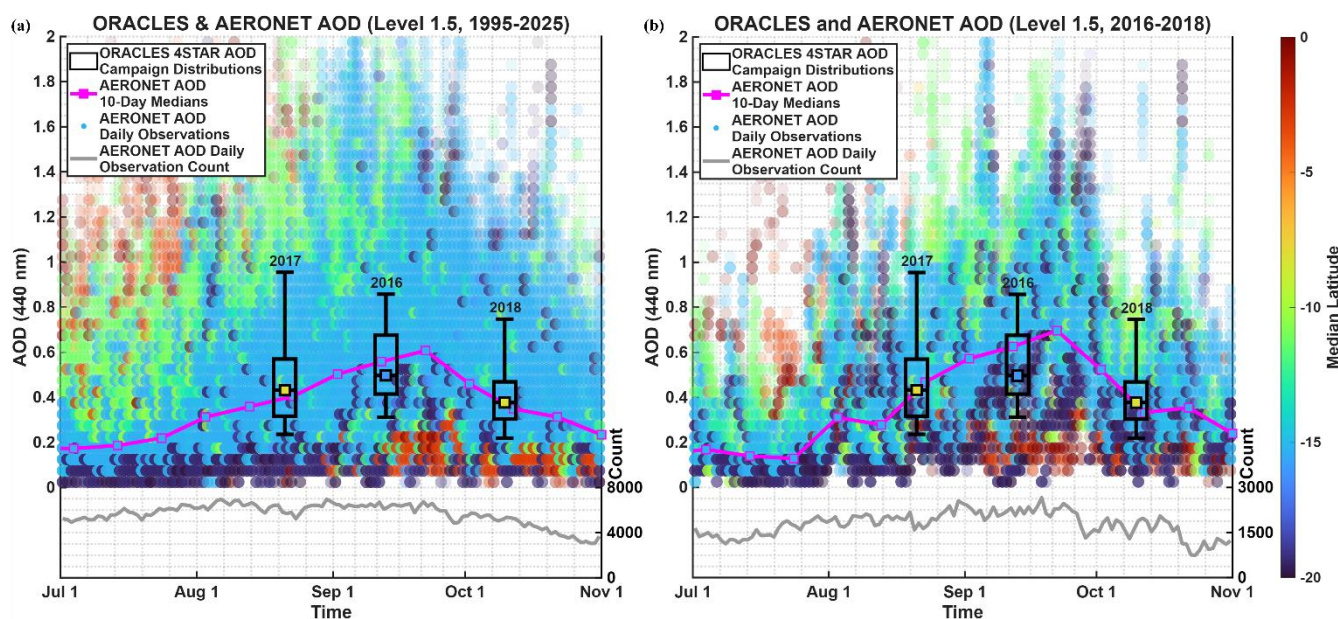
316 AOD peaks in September for both AERONET and 4STAR at 440 nm (Fig. 7), in agreement with the AOD trend
 317 from Fig. 3. Given that AOD is an extensive property, any conclusions drawn from 4STAR are dependent upon its sampling,
 318 e.g. when 4STAR operators chose to perform sky-scans and which sky-scans met the QC criteria. Thus, the agreement
 319 between 4STAR and AERONET may be somewhat coincidental but also suggests that 4STAR observed a similar
 320 distribution of aerosol loadings during sky-scan operation to that obtained by Southern African AERONET stations. The fact
 321 that 4STAR observed similar AOD to AERONET (i.e. not observing systematically lower values) implies that aerosol
 322 loading was generally conserved during early transport by the Southern African Easterly Jet. A possible mechanism for this
 323 is that any aerosol losses may have been compensated by water uptake and hygroscopic growth (Pistone et al., 2021; Pistone
 324 et al., 2024) as the aerosols were transported from drier land to moister ocean. Agreement is once again best for ORACLES
 325 2017 and 2018, which had greater sampling of the central smoke plume near 8 °S than the ORACLES 2016 campaign, which
 326 may account for the latter's AOD underestimate.

326

327 The greatest contributor of July-October AOD measurements is once again the AERONET station at Windpoort,
 328 Namibia (19.37 °S, 15.48 °E), supplying 14.7 % of 1995-2025 and 20.3 % of 2016-2018 data, with the latter percentage
 329 similarly increasing the station's visibility in Fig. 7b. The AERONET station at Mongu Inn, Zambia (15.27 °S, 23.13 °E) is
 330 the second greatest contributor of July-October AOD measurements for 1995-2025, supplying 14.3 % of the aerosol
 331 climatology, but is only third greatest for 2016-2018, supplying 14.0 % of the smaller dataset. However, since it is still
 centrally located within the latitudinal distribution of AERONET observations, it remains well-represented within both



332 panels of Fig. 7. The second greatest contributor of July-October AOD measurements for 2016-2018 is the AERONET
 333 station in Lubango, Namibia (14.96 °S, 13.45 °E), supplying 16.0 % of the smaller dataset, although its contributions are
 334 much more muted within the aerosol climatology, at only 8.4 %. The southward trend in African fires can be observed for
 335 AERONET AOD greater than 1.0, shifting from near the equator in July, to near 10 °S in August and September, to near 15
 336 °S in October, which is especially apparent in the climatology.



337
 338 **Figure 7: 4STAR AOD from ORACLES 2016-2018, with AERONET AOD for (a) 1995-2025 and (b) 2016-2018. Black boxes show**
 339 **4STAR’s interquartile range, with square medians, and whiskers extending to the 5th and 95th percentiles. AERONET 10-day**
 340 **medians (pink) are also shown. Background data are AERONET observations, with opacity weighted by count. The daily count of**
 341 **AERONET observations (gray) is also displayed at the bottom. All other colors represent the median latitude of the observations**
 342 **used to calculate each median SSA value or fill in each cell.**

343 4.2 Spatial Analyses

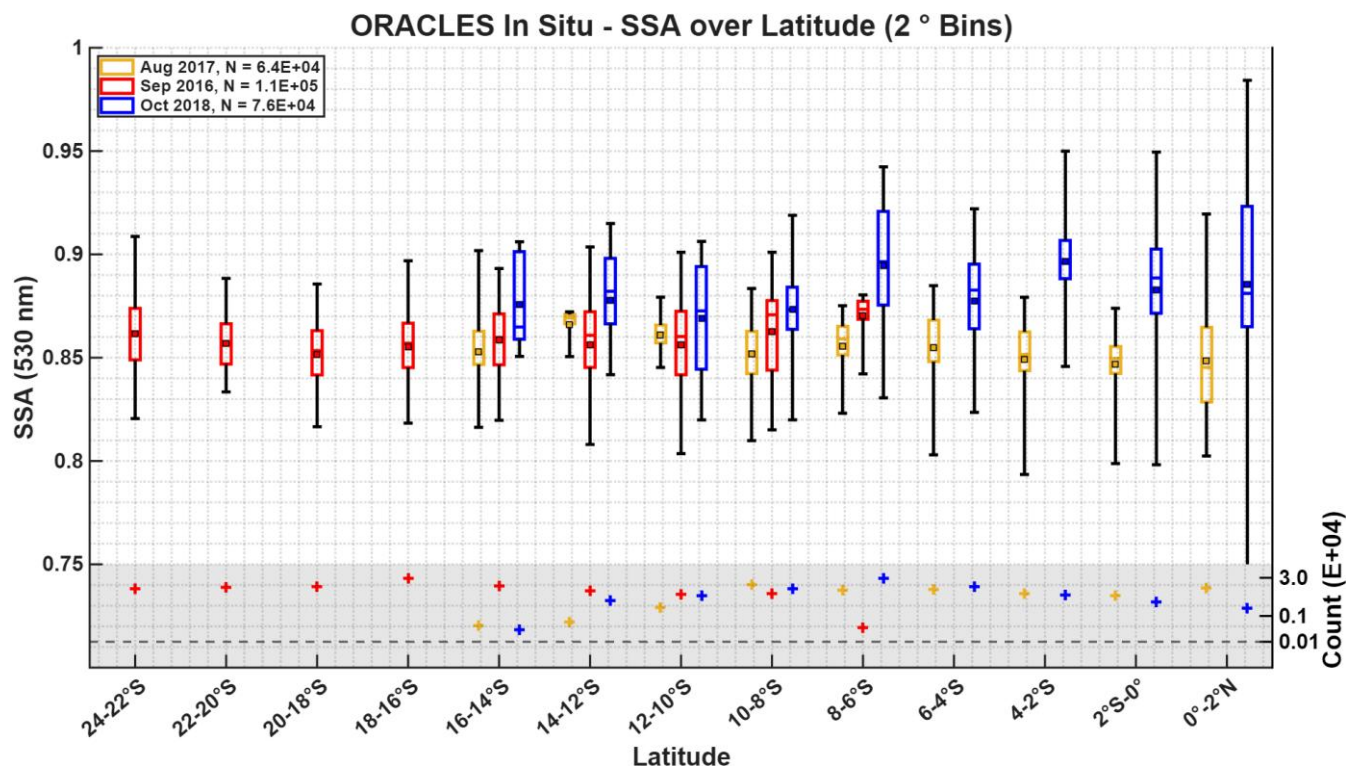
344 By binning SSA by latitude, longitude, and altitude, we can observe its spatial dependences. In situ SSA at 530 nm
 345 was chosen for these analyses due to its high volume of data points, as compared to the sparser 4STAR retrievals. For the
 346 latitudinal and longitudinal analyses, in situ SSA was binned by 2 °, while for the altitudinal analysis, it was binned by 0.5
 347 km. Each ORACLES campaign was kept separated, so that the subseasonal differences between in situ SSA values at each
 348 spatial bin could be observed.

349 The subseasonal increase in median SSA can be seen for latitudes spanning from 10 °S to 2 °N, with about a 0.03
 350 increase from August to October over that range (Fig. 8). For 10 - 6 °S, all three campaigns display the subseasonal increase,
 351 while only the ORACLES 2017 and 2018 campaigns can be observed over the 6 °S to 2 °N range. Over 14 - 10 °S, the SSA
 352 medians from August are greater than those from September, not aligning with the subseasonal increase, but August has
 353 much fewer samples than the other two campaigns at those latitudes, only containing 6 - 32 % as many datapoints.



354 For ORACLES 2016, median SSA increases by about 0.02 from 20 to 8 °S (excluding south of 20 °S due to
355 possible aerosol recirculations and 8 - 6 °S due to limited datapoints), indicating that ORACLES 2016 observed more
356 aerosol scattering as it approached the central smoke plume near 8 °S. Higher relative humidity near the equator can result in
357 higher SSA values (Ryoo et al., 2021; Dobracki et al., 2023) retrieved by AERONET or 4STAR, but the equatorward
358 increase of in situ SSA cannot solely be attributed to the higher relative humidity, as the PSAP optical block was heated to
359 30 - 50 °C and the relative humidity within the Nephys had an interquartile range of 6 to 40 % across the three campaigns
360 (Mitchell et al., 2026). This indicates a change in aerosol composition, which is reflective of the equatorward increase in
361 non-BC components noted by the back-trajectories of Dobracki et al. (2025). The aerosol compositional difference is likely
362 due to equatorward fires being smoldering and of woodier materials, generating more organic carbon.

363 Due to the relocation from Namibia to São Tomé, there are significant latitudinal differences between the
364 ORACLES 2016 and the ORACLES 2017-2018 campaigns. South of 14 °S contains 77 % of in situ measurements (and 82
365 % of sky-scans) for ORACLES 2016, but < 1 % of in situ measurements and sky-scans for ORACLES 2017 and 2018.
366 Conversely, north of 8 °S contains 70 - 71 % of in situ measurements (and 46 - 50 % of sky-scans) for ORACLES 2017 and
367 2018, but < 1 % of in situ measurements and sky-scans for ORACLES 2016. We subsampled 4STAR sky-scans from
368 ORACLES 2016 in the overlapping middle region of 14 to 8 °S to determine the effect of the southerly location of that
369 campaign on the SSA retrievals. Doing so yields a median SSA value of 0.86 at 500 nm for that region, which is 0.02 higher
370 than the ORACLES 2016 campaign median. This, combined with the northward increase in ORACLES 2016 in situ SSA
371 medians, suggests that if ORACLES 2016 had been similarly based out of São Tomé and sampled the central smoke plume
372 from the equator, 4STAR and in situ SSA would likely have been higher overall, with greater similarity to AERONET
373 observations and more in alignment with the subseasonal SSA increase.



374

375 **Figure 8: In situ SSA for ORACLES 2016-2018, binned by 2 ° latitude. The ORACLES 2016 (September) campaign is centered,**
 376 **with ORACLES 2017 (August) jittered to its left and ORACLES 2018 (October) to its right. Boxes show the interquartile range,**
 377 **while whiskers extend to the 5th and 95th percentiles. Central lines are medians and squares are means. Observation counts per**
 378 **bin are displayed at the bottom.**

379

380

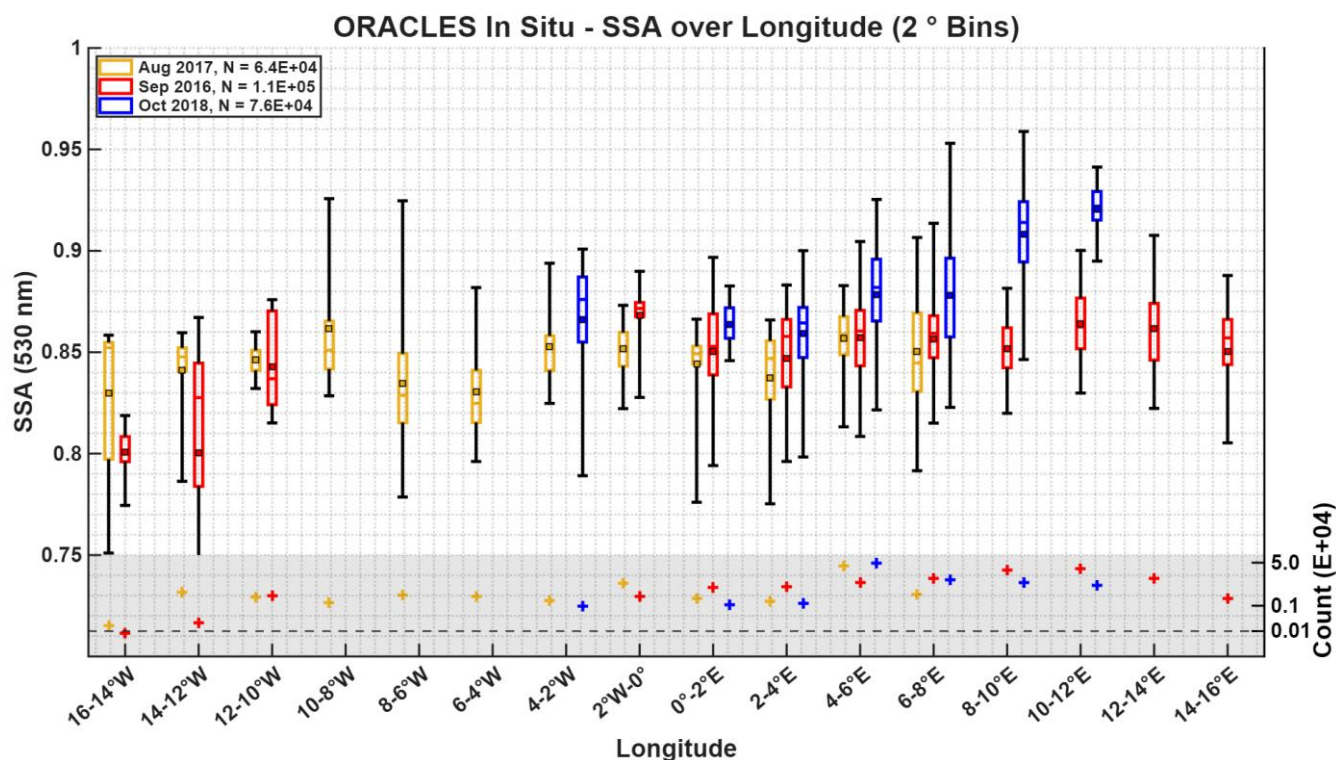
381 The month-to-month increase in median SSA can also be seen for longitudes spanning from 4 °W to 12 °E, with
 382 about a 0.03 increase over that range (Fig. 9). For 0 ° to 8 °E, all three campaigns display the subseasonal increase, while
 383 only two campaigns can be observed for 4 °W to 0 ° and 8 to 12 °E. The longitudes of 12 - 16 °E were only observed by
 384 ORACLES 2016, while 10 - 4 °W were only observed by ORACLES 2017, not allowing for a subseasonal analysis.

385

386 In the eastern portion of the basin (16 °E to 2 °W), ORACLES 2016 median SSA is centered near 0.86, with a bin-
 387 to-bin variability of about 0.01. Between 10 and 16 °W, ORACLES 2016 median SSA decreases from about 0.84 to 0.80,
 388 reflecting a similar SSA decrease found by Fakoya et al. (2025) for aged free tropospheric BBA over the Southeast Atlantic.
 389 They attribute this SSA decrease to aerosol aging processes, such as a lensing effect, whereby organic aerosol coatings focus
 390 more light on the BC core and increase BBA absorptivity (Taylor et al., 2020), and/or a loss of organic aerosol coating via
 391 heterogeneous oxidation and subsequent reduction of BBA scattering (Sedlacek et al., 2022). Over the central portion of the
 392 basin (8 °E to 4 °W), ORACLES 2017 median SSA remains almost constant near 0.85, with a bin-to-bin variability of about
 393 0.01. This declines to about 0.83 over 4 - 8 °W, which rebounds to 0.85 for 8 - 16 °W, aligning with the transition from nine-
 day to eleven-day aged aerosols described by Fakoya et al. (2025). For the east-central portion of the basin (12 °E to 0 °),
 ORACLES 2018 median SSA decreases westward from about 0.92 to 0.86, then rebounds to 0.88 at 2 - 4 °W. This suggests

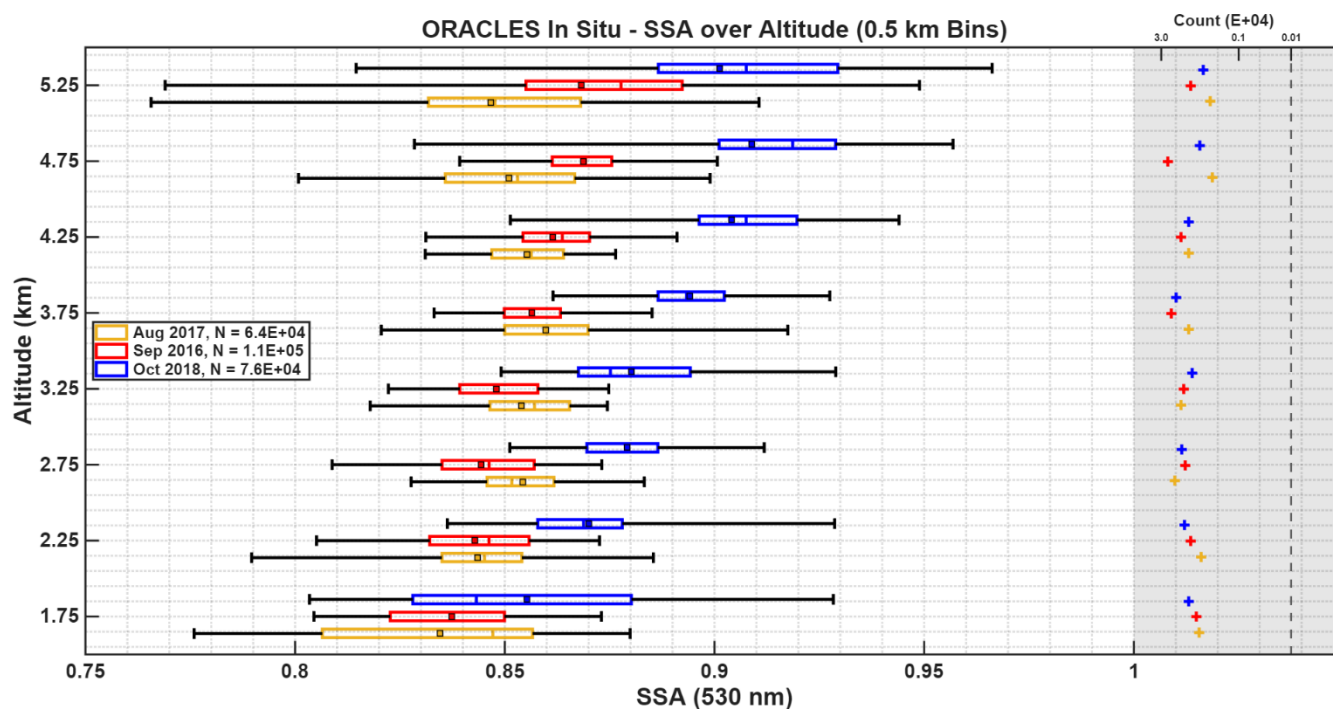


394 that the aerosol aging processes from Fakoya et al. (2025) occurred much further east for ORACLES 2018 than the other two
 395 campaigns. This aligns with the southeastward shift of fires in October, allowing more time for aerosol aging processes to
 396 occur before arriving in the ORACLES study region over the Southeast Atlantic.



397
 398 **Figure 9: In situ SSA for ORACLES 2016-2018, binned by 2° longitude. The ORACLES 2016 (September) campaign is centered,**
 399 **with ORACLES 2017 (August) jittered to its left and ORACLES 2018 (October) to its right. Boxes show the interquartile range,**
 400 **while whiskers extend to the 5th and 95th percentiles. Central lines are medians and squares are means. Observation counts per**
 401 **bin are displayed at the bottom.**

402
 403 SSA generally increases with altitude for all three ORACLES campaigns (Fig. 10), in agreement with Fig. 14 from
 404 Redemann et al. (2021), with an average increase of about 0.04 per campaign over the entire free-tropospheric range of 1.5 -
 405 5.5 km. The subseasonal increase in median SSA is strongest in the upper portion of the smoke plume (4 - 5.5 km), with all
 406 three campaigns in ascending order and an increase of about 0.05 from August to October over that span. September median
 407 SSA is lower than August within the lower portion of the smoke plume (2 - 4 km), but there is still an increase of about 0.03
 408 from August to October. Altitudinal increases in SSA have been attributed to increases in ammonium (NH₃) with altitude
 409 (Wu et al., 2020), although not much NH₃ has been measured in the region, estimated to be about 5 % of the mean
 410 submicron mass spectrum by Dobracki et al. (2023). The altitudinal increase in SSA is also correlated with a general
 411 decrease in the black carbon to organic aerosol ratio with height (Redemann et al., 2021). Another possibility is that stronger
 412 winds at higher altitudes result in fresher aerosols aloft, compared to chemically aged aerosols below.



413

414 **Figure 10: In situ SSA for ORACLES 2016-2018, binned by 0.5 km altitude. Ticks represent the altitudinal center of the bin. The**
 415 **ORACLES 2016 (September) campaign is centered, with ORACLES 2017 (August) jittered below it and ORACLES 2018**
 416 **(October) above it. Boxes show the interquartile range, while whiskers extend to the 5th and 95th percentiles. Central lines are**
 417 **medians and squares are means. Observation counts per bin are displayed on the right.**

418 5 Conclusions

419 A subseasonal increase in SSA from 4STAR retrievals and in situ measurements during ORACLES 2016-2018
 420 indicates that biomass burning aerosols over the Southeast Atlantic experience an aerosol brightening process over the
 421 course of the BBA emission season. The subseasonal SSA increase is likely to increase critical albedo, which decreases
 422 DARE and reduces heating rates in clear and partially cloudy conditions, weakening atmospheric stability. The SSA increase
 423 from ORACLES over-ocean observations is also consistent with the near-source observations from Southern African
 424 AERONET stations, which have recently reached 30 years of continuous operation, allowing for analysis of a complete
 425 aerosol climatology for the first time. EAE and AAE have little subseasonal variation, indicating domination by fine BC
 426 aerosols throughout the season, suggesting that the aerosol brightening is due to a change in aerosol composition through the
 427 season, rather than a change in aerosol type. Further expansion of the 4STAR dataset into the UV spectrum via the use of
 428 hyperspectral GRASP (Generalized Retrieval of Atmosphere and Surface Properties) code (Román et al., 2018) would help
 429 to confirm this via improved identification of BrC absorption, which is the subject of ongoing work. Regarding the complex
 430 refractive indices, the decrease in IRI is relatively greater than the concurrent decrease in RRI, suggesting that the aerosol



431 brightening depends more upon a decrease in aerosol absorptivity, rather than an actual increase in scattering. 4STAR
432 retrievals of AOD and AAOD both peak in September, which is also reflected in the AERONET data. These results are in
433 line with the previously reported pattern of BBA emissions across the source regions.

434 SSA medians from ORACLES 4STAR retrievals and in situ measurements agree well with those from AERONET,
435 indicating that the BBA radiative properties observed over the Southeast Atlantic are still largely reflective of those emitted
436 from the source region of Southern Africa, with both experiencing a similar subseasonal increase in SSA from aerosol
437 brightening. There is also agreement in AOD medians between ORACLES and AERONET, suggesting that any aerosol
438 losses during transport by the Southern African Easterly Jet may have been compensated by water uptake and hygroscopic
439 growth. The general agreement between these two adjacent regions showcases the relevance of the ORACLES dataset even
440 outside of its direct study area. This is true for both the concurrent campaign years and the full AERONET aerosol
441 climatology, highlighting the ability of ORACLES observations to reflect long term trends.

442 The SSA and AOD medians retrieved by 4STAR during the ORACLES 2016 campaign are generally lower than
443 the respective AERONET medians. A latitudinal analysis of in situ measurements and subsampling of 4STAR sky-scans
444 suggests that ORACLES 2016 would likely have observed greater scattering if it had targeted the central smoke plume from
445 the equator like the other two campaigns, which would have brought the 4STAR SSA medians more in line with the
446 subseasonal increase observed by AERONET. The equatorward increase in SSA also aligns with findings that the source
447 fires within that region are smoldering and of woodier materials. Increased observation of the central smoke plume by
448 ORACLES 2016 would likely have yielded higher aerosol loadings, also bringing AOD into greater agreement with
449 AERONET.

450 Each campaign observed a westward gradual increase in SSA, followed by a sharper decline, and (in two cases) a
451 subsequent rebound, aligning with late-transport aging processes identified by previous studies, attributed to a lensing effect
452 and/or reduction of organic aerosol coating. This process appears to have occurred much further east for ORACLES 2018,
453 aligning with the southeastward shift of fires in October, allowing more time for aerosol aging processes to occur before
454 arriving to the Southeast Atlantic. SSA generally increases with altitude, in agreement with previous studies, which is
455 attributed to either increasing ammonium, decreasing the black carbon to organic aerosol ratio, or stronger winds keeping
456 fresher aerosols aloft. The subseasonal SSA increase can be seen throughout the free-tropospheric vertical column but is
457 strongest in the upper portion of the smoke plume. 4STAR retrievals and in situ measurements were adept at identifying
458 subseasonal aerosol brightening during the ORACLES campaigns over the Southeast Atlantic, a critical study region that can
459 otherwise be quite difficult to observe.



460 **Data Availability:**

461 NASA ORACLES P-3 4STAR aerosol inversions and in situ absorption measurements are accessible via:

462 https://doi.org/10.5067/ASDC_DAAC/ORACLES_Aerosol_AircraftInSitu_Data_1 (NASA/LARC/SD/ASDC, 2020).

463 AERONET AOD and aerosol inversions are accessible via: <https://aeronet.gsfc.nasa.gov/> (NASA GSFC, 2026).

464 **Author Contributions**

465 All figures were created by LTM, under the guidance of CJF and JR, and with input from KP and SEL. PZ and RW were PIs
466 for ORACLES Mission Science. JR and SEL were PIs for 4STAR during ORACLES 2016 and ORACLES 2017-2018,
467 respectively. KSS was the PI for SSFR during ORACLES. KP and SEL operated the 4STAR instrument aboard the P-3
468 aircraft for all of ORACLES, while CJF also operated during ORACLES 2016. LTM prepared the manuscript with
469 contributions from all co-authors.

470 **Competing Interests**

471 The authors declare that they have no conflict of interest.

472 **Acknowledgements**

473 We thank the NASA ORACLES team for a successful mission. Data analysis and visualization were conducted utilizing
474 MATLAB. Mapping was performed using QGIS.

475 **Financial Support**

476 This research was supported by the NASA Atmosphere Observing System (AOS) mission (grant no. 80NSSC23M0083). It
477 was also supported by the University of Oklahoma (OU) start-up package (grant no. 122007900). The ORACLES field
478 campaign was funded through the NASA Earth Venture Suborbital-2 program (grant no. NNH13ZDA001N-EVS2).

479 **References**

480 Abel, S. J., Haywood, J. M., Highwood, E. J., Li, J., and Buseck, P. R.: Evolution of biomass burning aerosol properties
481 from an agricultural fire in southern Africa, *Geophys. Res. Lett.*, 30, 1783, <https://doi.org/10.1029/2003GL017342>, 2003.

482

483 Adebisi, A. A., and Zuidema, P.: The role of the southern African easterly jet in modifying the southeast Atlantic aerosol a
484 and cloud environments, *Q. J. Roy. Meteorol. Soc.*, 142, 1574–1589, <https://doi.org/10.1002/qj.2765>, 2016



- 485 Adebisi, A., Zuidema, P., and Abel, S.: The convolution of dynamics and moisture with the presence of shortwave absorbing
486 aerosols over the southeast Atlantic, *J. Climate*, 28, 1997–2024, <https://doi.org/10.1175/JCLI-D-14-00352.1>, 2015.
- 487
- 488 Alexander, D. T. L., Crozier, P. A., and Anderson, J. R.: Brown carbon spheres in East Asian outflow and their optical
489 properties, *Science*, 321, 833–836, <https://doi.org/10.1126/science.1155296>, 2008.
- 490
- 491 Anderson, T. L., and Ogren, J. A.: Determining aerosol radiative properties using the TSI 3563 integrating nephelometer,
492 *Aerosol Sci. Tech.*, 29, 1, 57–69, <https://doi.org/10.1080/02786829808965551>, 1998.
- 493
- 494 Bellouin, N., Quaas, J., Gryspeerdt, E., Kinne, S., Stier, P., Watson-Parris, D., Boucher, O., Carslaw, K. S., Christensen, M.,
495 Daniau, A.-L., Dufresne, J.-L., Feingold, G., Fiedler, S., Forster, P., Gettelman, A., Haywood, J. M., Lohmann, U.,
496 Malavelle, F., Mauritsen, T., McCoy, D. T., Myhre, G., Mülmstädt, J., Neubauer, D., Possner, A., Rugenstein, M., Sato,
497 Y., Schulz, M., Schwartz, S. E., Sourdeval, O., Storelvmo, T., Toll, V., Winker, D., and Stevens, B.: Bounding global
498 aerosol radiative forcing of climate change, *Rev. Geophys.*, 58, e2019RG000660, <https://doi.org/10.1029/2019RG000660>,
499 2020.
- 500
- 501 Bergstrom, R. W., Pilewskie, P., Russell, P. B., Redemann, J., Bond, T. C., Quinn, P. K., and Sierau, B.: Spectral absorption
502 properties of atmospheric aerosols, *Atmos. Chem. Phys.*, 7, 5937–5943, <https://doi.org/10.5194/acp-7-5937-2007>, 2007.
- 503
- 504 Bond, T. C., Doherty, S. J., Fahey, D. W., Forster, P. M., Berntsen, T., DeAngelo, B. J., Flanner, M. G., Ghan, S., Kärcher,
505 B., Koch, D., Kinne, S., Kondo, Y., Quinn, P. K., Sarofim, M. C., Schultz, M. G., Schulz, M., Venkataraman, C., Zhang, H.,
506 Zhang S., Bellouin, N., Guttikunda, S. K., Hopke, P. K., Jacobson, M. Z., Kaiser, J. W., Klimont, Z., Lohmann, U., Schwarz,
507 J. P., Shindell, D., Storelvmo, T., Warren, S. G., and Zender, C. S.: Bounding the role of black carbon in the climate system:
508 A scientific assessment, *J. Geophys. Res.-Atmos.*, 118, 5380–5552, <https://doi.org/10.1002/jgrd.50171>, 2013.
- 509
- 510 Bowman, D. M. J. S., Balch, J. K., Artaxo, P., Bond, W. J., Carlson, J. M., Cochrane, M. A., D'Antonio, C. M., DeFries, R.
511 S., Doyle, J. C., Harrison, S. P., Johnston, F. H., Keeley, J. E., Krawchuk, M. A., Kull, C. A., Marston, J. B., Moritz, M. A.,
512 Prentice, I. C., Roos, C. I., Scott, A. C., Swetnam, T. W., van der Werf, G. R., and Pyne, S. J.: Fire in the earth system,
513 *Science*, 324, 481–484, <https://doi.org/10.1126/science.1163886>, 2009.
- 514
- 515 Brown, H., Liu, X., Pokhrel, K., Murphy, S., Lu, Z., Saleh, R., Mielonen, T., Kokkola, H., Bergman, T., Myhre, G., Skeie,
516 R. B., Watson-Paris, D., Stier, P., Johnson, B., Bellouin, N., Schulz, M., Vakkari, V., Beukes, J. P., van Zyl, P. G., Liu, S.,
517 and Chand D.: Biomass burning aerosols in most climate models are too absorbing, *Nat. Commun.*, 12, 277,
518 <https://doi.org/10.1038/s41467-020-20482-9>, 2021.
- 519
- 520 Brown, S. W., Johnson, B. C., Biggar, S. F., Zalewski, E. F., Cooper, J., Hajek, P., Hildum, E., Grant, P., Barnes, R. A., and
521 Butler, J. J.: Radiometric validation of NASA's Ames Research Center's Sensor Calibration Laboratory, *Appl. Optics*, 44,
522 6426–6443, <https://doi.org/10.1364/AO.44.006426>, 2005.
- 523
- 524 Chand, D., Wood, R., Anderson, T. L., Satheesh, S. K., and Charlson, R. J.: Satellite-derived direct radiative effect of
525 aerosols dependent on cloud cover, *Nat. Geosci.*, 2, 181–184, <https://doi.org/10.1038/ngeo437>, 2009.
- 526
- 527 Che, H., Stier, P., Gordon, H., Watson-Parris, D., and Deaconu, L.: Cloud adjustments dominate the overall negative aerosol
528 radiative effects of biomass burning aerosols in UKESM1 climate model simulations over the south-eastern Atlantic, *Atmos.*
529 *Chem. Phys.*, 21, 17–33, <https://doi.org/10.5194/acp-21-17-2021>, 2021.
- 530
- 531 Choi, M., Lyapustin, A., Schuster, G. L., Go, S., Wang, Y., Korkin, S., Kahn, R., Reid, J. S., Hyer, E. J., Eck, T. F., Chin,
532 M., Diner, D. J., Kalashnikova, O., Dubovik, O., Kim, J., and Moosmüller, H.: Light-absorbing black carbon and brown
533 carbon components of smoke aerosol from DSCOVR EPIC measurements over North America and central Africa, *Atmos.*
534 *Chem. Phys.*, 24, 10543–10565, <https://doi.org/10.5194/acp-24-10543-2024>, 2024.



- 535 Cochrane, S. P., Schmidt, K. S., Chen, H., Pilewskie, P., Kittelman, S., Redemann, J., LeBlanc, S., Pistone, K.,
536 Kacenelenbogen, M., Segal Rozenhaimer, M., Shinozuka, Y., Flynn, C., Platnick, S., Meyer, K., Ferrare, R., Burton, S.,
537 Hostetler, C., Howell, S., Freitag, S., Dobracki, A., and Doherty, S.: Above-cloud aerosol radiative effects based on
538 ORACLES 2016 and ORACLES 2017 aircraft experiments, *Atmos. Meas. Tech.*, 12, 6505–6528,
539 <https://doi.org/10.5194/amt-12-6505-2019>, 2019.
- 540
541 Cochrane, S. P., Schmidt, K. S., Chen, H., Pilewskie, P., Kittelman, S., Redemann, J., LeBlanc, S., Pistone, K.,
542 Kacenelenbogen, M., Segal Rozenhaimer, M., Shinozuka, Y., Flynn, C., Dobracki, A., Zuidema, P., Howell, S., Freitag, S.,
543 and Doherty, S.: Empirically derived parameterizations of the direct aerosol radiative effect based on ORACLES aircraft
544 observations, *Atmos. Meas. Tech.*, 14, 567–593, <https://doi.org/10.5194/amt-14-567-2021>, 2021.
- 545
546 Cochrane, S. P., Schmidt, K. S., Chen, H., Pilewskie, P., Kittelman, S., Redemann, J., LeBlanc, S., Pistone, K., Segal
547 Rozenhaimer, M., Kacenelenbogen, M., Shinozuka, Y., Flynn, C., Ferrare, R., Burton, S., Hostetler, C., Mallet, M., and
548 Zuidema, P.: Biomass burning aerosol heating rates from the ORACLES (ObseRvations of Aerosols above CLouds and their
549 intEractionS) 2016 and 2017 experiments, *Atmos. Meas. Tech.*, 15, 61–77, <https://doi.org/10.5194/amt-15-61-2022>, 2022.
- 550
551 Coddington, O., Schmidt, K. S., Pilewskie, P., Gore, W. J., Bergstrom, R. W., Román, M., Redemann, J., Russell, P. B., Liu,
552 J., and Schaaf, C. C.: Aircraft measurements of spectral surface albedo and its consistency with ground-based and space-
553 borne observations, *J. Geophys. Res.-Atmos.*, 113, D17, <https://doi.org/10.1029/2008JD010089>, 2008.
- 554
555 Collier, S., Zhou, S., Onasch, T. B., Jaffe, D. A., Kleinman, L., Sedlacek III, A. J., Briggs, N. L., Hee, J., Fortner, E.,
556 Shilling, J. E., Worsnop, D., Yokelson, R. J., Parworth, C., Ge, X., Xu, J., Butterfield, Z., Chand, D., Dubey, M. K., Pekour,
557 M. S., Springston, S., and Zhang, Q.: Regional influence of aerosol emissions from fires driven by combustion efficiency:
558 Insights from the BBOP campaign, *Environ. Sci. Technol.*, 50, 8613–8622, <https://doi.org/10.1021/acs.est.6b01617>, 2016.
- 559
560 Dang, C., Segal-Rozenhaimer, M., Che, H., Zhang, L., Formenti, P., Taylor, J., Dobracki, A., Purdue, S., Wong, P.-S.,
561 Nenes, A., Sedlacek III, A., Coe, H., Redemann, J., Zuidema, P., Howell, S., and Haywood, J.: Biomass burning and marine
562 aerosol processing over the southeast Atlantic Ocean: a TEM single-particle analysis, *Atmos. Chem. Phys.*, 22, 9389–9412,
563 <https://doi.org/10.5194/acp-22-9389-2022>, 2022.
- 564
565 de Graaf, M., Bellouin, N., Tilstra, L. G., Haywood, J., and Stammes, P.: Aerosol direct radiative effect of smoke over
566 clouds over the southeast Atlantic Ocean from 2006 to 2009, *Geophys. Res. Lett.*, 41, 7723–7730,
567 <https://doi.org/10.1002/2014GL061103>, 2014.
- 568
569 Denjean, C., Brito, J., Libois, Q., Mallet, M., Bourriane, T., Burnet, F., Dupuy, R., Flamant, C., and Knippertz, P.:
570 Unexpected biomass burning aerosol absorption enhancement explained by black carbon mixing state, *Geophys. Res. Lett.*,
571 47, e2020GL089055, <https://doi.org/10.1029/2020GL089055>, 2020.
- 572
573 Dobracki, A., Zuidema, P., Howell, S. G., Saide, P., Freitag, S., Aiken, A. C., Burton, S. P., Sedlacek III, A. J., Redemann,
574 J., and Wood, R.: An attribution of the low single-scattering albedo of biomass burning aerosol over the southeastern
575 Atlantic, *Atmos. Chem. Phys.*, 23, 4775–4799, <https://doi.org/10.5194/acp-23-4775-2023>, 2023.
- 576
577 Dobracki, A., Lewis, E. R., Sedlacek III, A. J., Tatro, T., Zawadowicz, M. A., and Zuidema, P.: Burning conditions and
578 transportation pathways determine biomass-burning aerosol properties in the Ascension Island marine boundary layer,
579 *Atmos. Chem. Phys.*, 25, 2333–2363, <https://doi.org/10.5194/acp-25-2333-2025>, 2025.



- 580 Doherty, S. J., Saide, P. E., Zuidema, P., Shinozuka, Y., Ferrada, G. A., Gordon, H., Mallet, M., Meyer, K., Painemal, D.,
581 Howell, S. G., Freitag, S., Dobracki, A., Podolske, J. R., Burton, S. P., Ferrare, R. A., Howes, C., Nabat, P., Carmichael, G.
582 R., da Silva, A., Pistone, K., Chang, I., Gao, L., Wood, R., and Redemann, J.: Modeled and observed properties related to the
583 direct aerosol radiative effect of biomass burning aerosol over the southeastern Atlantic, *Atmos. Chem. Phys.*, 22, 1–46,
584 <https://doi.org/10.5194/acp-22-1-2022>, 2022.
- 585
586 Dubovik, O., and King, M. D.: A flexible inversion algorithm for retrieval of aerosol optical properties from Sun and sky
587 radiance measurements, *J. Geophys. Res.-Atmos.*, 105, 20673–20696, <https://doi.org/10.1029/2000JD900282>, 2000.
- 588
589 Dunagan, S. E., Johnson, R., Zavaleta, J., Russell, P. B., Schmid, B., Flynn, C., Redemann, J., Shinozuka, Y., Livingston, J.,
590 Segal-Rosenhaimer, M.: Spectrometer for Sky-Scanning Sun-Tracking Atmospheric Research (4STAR): Instrument
591 Technology, *Remote Sens.*, 5, 3872–3895, <https://doi.org/10.3390/rs5083872>, 2013.
- 592
593 Eck, T. F., Holben, B. N., Reid, J. S., Mukelabai, M. M., Piketh, S. J., Torres, O., Jethva, H. T., Hyer, E. J., Ward, D. E.,
594 Dubovik, O., Sinyuk, A., Schafer, J. S., Giles, D. M., Sorokin, M., Smirnov, A., and Slutsker, I.: A seasonal trend of single
595 scattering albedo in southern African biomass-burning particles: Implications for satellite products and estimates of
596 emissions for the world's largest biomass-burning source, *J. Geophys. Res.-Atmos.*, 118, 6414–6432,
597 <https://doi.org/10.1002/jgrd.50500>, 2013.
- 598
599 Fakoya, A. A., Redemann, J., Saide, P. E., Gao, L., Mitchell, L. T., Howes, C., Dobracki, A., Chang, I., Ferrada, G. A.,
600 Pistone, K., Leblanc, S. E., Segal-Rosenhaimer, M., Sedlacek III, A. J., Eck, T., Holben, B., Gupta, P., Lind, E., Zuidema,
601 P., Carmichael, G., and Flynn, C. J.: Atmospheric processing and aerosol aging responsible for observed increase in
602 absorptivity of long-range-transported smoke over the southeast Atlantic, *Atmos. Chem. Phys.*, 25, 7879–7902,
603 <https://doi.org/10.5194/acp-25-7879-2025>, 2025.
- 604
605 Formenti, P., D'Anna, B., Flamant, C., Mallet, M., Piketh, S. J., Schepanski, K., Waquet, F., Auriol, F., Brogniez, G., Burnet,
606 F., Chaboureaud, J.-P., Chauvigné, A., Chazette, P., Denjean, C., Desboeufs, K., Doussin, J.-F., Elguindi, N., Feuerstein, S.,
607 Gaetani, M., Giorio, C., Klopfer, D., Mallet, M. D., Nabat, P., Monod, A., Solmon, F., Namwoonde, A., Chikwililwa, C.,
608 Mushi, R., Welton, E. J., and Holben, B.: The Aerosols, Radiation and Clouds in Southern Africa field campaign in
609 Namibia: Overview, illustrative observations, and way forward, *B. Am. Meteorol. Soc.*, 100, 1277–1298,
610 <https://doi.org/10.1175/bams-d-17-0278.1>, 2019.
- 611
612 Giles, D. M., Sinyuk, A., Sorokin, M. G., Schafer, J. S., Smirnov, A., Slutsker, I., Eck, T. F., Holben, B. N., Lewis, J. R.,
613 Campbell, J. R., Welton, E. J., Korokin, S. V., and Lyapustin, A. I.: Advancements in the Aerosol Robotic Network
614 (AERONET) Version 3 database – automated near-real-time quality control algorithm with improved cloud screening for
615 Sun photometer aerosol optical depth (AOD) measurements, *Atmos. Meas. Tech.*, 12, 169–209, <https://doi.org/10.5194/amt-12-169-2019>, 2019.
- 616
617
618 Granier, C., Bessagnet, B., Bond, T., D'Angiola, A., Denier van der Gon, H., Frost, G. J., Heil, A., Kaiser, J. W., Kinne, S.,
619 Klimont, Z., Kloster, S., Lamarque, J.-F., Liousse, C., Masui, T., Meleux, F., Mieville, A., Ohara, T., Raut, J.-C., Riahi, K.,
620 Schultz, M. G., Smith, S. J., Thompson, A., van Aardenne, J., van der Werf, G. R., and van Vuuren, D. P.: Evolution of
621 anthropogenic and biomass burning emissions of air pollutants at global and regional scales during the 1980–2010 period,
622 *Climatic Change*, 109, 163, <https://doi.org/10.1007/s10584-011-0154-1>, 2011.
- 623
624 Haywood, J. M., Abel, S. J., Barrett, P. A., Bellouin, N., Blyth, A., Bower, K. N., Brooks, M., Carslaw, K., Che, H., Coe, H.,
625 Cotterell, M. I., Crawford, I., Cui, Z., Davies, N., Dingley, B., Field, P., Formenti, P., Gordon, H., de Graaf, M., Herbert, R.,
626 Johnson, B., Jones, A. C., Langridge, J. M., Malavelle, F., Partridge, D. G., Peers, F., Redemann, J., Stier, P., Szpek, K.,
627 Taylor, J. W., Watson-Parris, D., Wood, R., Wu, H., and Zuidema, P.: The Cloud-Aerosol-Radiation Interaction and
628 Forcing: Year 2017 (CLARIFY-2017) measurement campaign, *Atmos. Chem. Phys.*, 21, 1049–1084,
629 <https://doi.org/10.5194/acp-21-1049-2021>, 2021.



- 630 Holanda, B. A., Pöhlker, M. L., Walter, D., Saturno, J., Sörgel, M., Ditas, J., Ditas, F., Schulz, C., Franco, M. A., Wang, Q.,
631 Donth, T., Artaxo, P., Barbosa, H. M. J., Borrmann, S., Braga, R., Brito, J., Cheng, Y., Dollner, M., Kaiser, J. W., Klimach,
632 T., Knote, C., Krüger, O. O., Fütterer, D., Lavrič, J. V., Ma, N., Machado, L. A. T., Ming, J., Morais, F. G., Paulsen, H.,
633 Sauer, D., Schlager, H., Schneider, J., Su, H., Weinzierl, B., Walser, A., Wendisch, M., Ziereis, H., Zöger, M., Pöschl, U.,
634 Andreae, M. O., and Pöhlker, C.: Influx of African biomass burning aerosol during the Amazonian dry season through
635 layered transatlantic transport of black carbon-rich smoke, *Atmos. Chem. Phys.*, 20, 4757–4785, [https://doi.org/10.5194/acp-](https://doi.org/10.5194/acp-20-4757-2020)
636 [20-4757-2020](https://doi.org/10.5194/acp-20-4757-2020), 2020.
- 637
- 638 Holben, B. N., Eck, T. F., Slutsker, I., Tanré, D., Buis, J. P., Setzer, A., Vermote, E., Reagan, J. A., Kaufman, Y. J.,
639 Nakajima, T., Lavenu, F., Jankowiak, I., and Smirnov, A.: AERONET – A federated instrument network and data archive
640 for aerosol characterization, *Remote Sens. Environ.*, 66, 1–16, [https://doi.org/ 10.1016/S0034-4257\(98\)00031-5](https://doi.org/10.1016/S0034-4257(98)00031-5), 1998.
- 641
- 642 Holben, B. N., Eck, T. F., Slutsker, I., Smirnov, A., Sinyuk, A., Schafer, J. S., Giles, D. M., and Dubovik, O.: AERONET's
643 version 2.0 quality assurance criteria, *Remote Sensing of Atmosphere and Clouds*, Proc. SPIE, 6408, 64080Q,
644 <https://doi.org/10.1117/12.706524>, 2006.
- 645
- 646 Keil, A. and Haywood, J. M.: Solar radiative forcing by biomass burning aerosol particles during SAFARI 2000: A case
647 study based on measured aerosol and cloud properties, *J. Geophys. Res.-Atmos.*, 108, 8467,
648 <https://doi.org/10.1029/2002JD002315>, 2003.
- 649
- 650 Jen, C. N., Hatch, L. E., Selimovic, V., Yokelson, R. J., Weber, R., Fernandez, A. E., Kreisberg, N. M., Barsanti, K. C., and
651 Goldstein, A. H.: Speciated and total emission factors of particulate organics from burning western US wildland fuels and
652 their dependence on combustion efficiency, *Atmos. Chem. Phys.*, 19, 1013–1026, <https://doi.org/10.5194/acp-19-1013-2019>,
653 2019.
- 654
- 655 Jethva, H. T., Torres, O., Ferrare, R. A., Burton, S. P., Cook, A. L., Harper, D. B., Hostetler, C. A., Redemann, J., Kayetha,
656 V., LeBlanc, S., Pistone, K., Mitchell, L., and Flynn, C. J.: Retrieving UV-Vis spectral single-scattering albedo of absorbing
657 aerosols above clouds from synergy of ORACLES airborne and A-train sensors, *Atmos. Meas. Tech.*, 17, 2335–2366,
658 <https://doi.org/10.5194/amt-17-2335-2024>, 2024.
- 659
- 660 LeBlanc, S. E., Redemann, R., Flynn, C., Pistone, K., Kacenelenbogen, M., Segal-Rosenheimer, M., Shinozuka, Y.,
661 Dunagan, S., Dahlgren, R. P., Meyer, K., Podolske, J., Howell, S. G., Freitag, S., Small-Griswold, J., Holben, B., Diamond,
662 M., Wood, R., Formenti, P., Piketh, S., Maggs-Kölling, G., Gerber, M., and Namwoonde, A.: Above-cloud aerosol optical
663 depth from airborne observations in the southeast Atlantic, *Atmos. Chem. Phys.*, 20, 1565–1590, [https://doi.org/10.5194/acp-](https://doi.org/10.5194/acp-20-1565-2020)
664 [20-1565-2020](https://doi.org/10.5194/acp-20-1565-2020), 2020.
- 665
- 666 Levin, E. J. T., McMeeking, G. R., Carrico, C. M., Mack, L. E., Kreidenweis, S. M., Wold, C. E., Moosmüller, H., Arnott,
667 W. P., Hao, W. M., Collett Jr., J. L., and Malm, W. C.: Biomass burning smoke aerosol properties measured during Fire
668 Laboratory at Missoula Experiments (FLAME), *J. Geophys. Res.-Atmos.*, 115, D18210,
669 <https://doi.org/10.1029/2009JD013601>, 2010.
- 670
- 671 Mallet, M., Solmon, F., Nabat, P., Elguindi, N., Waquet, F., Bouniol, D., Sayer, A. M., Meyer, K., Roehrig, R., Michou, M.,
672 Zuidema, P., Flamant, C., Redemann, J., and Formenti, P.: Direct and semi-direct radiative forcing of biomass-burning
673 aerosols over the southeast Atlantic (SEA) and its sensitivity to absorbing properties: a regional climate modeling study,
674 *Atmos. Chem. Phys.*, 20, 13191–13216, <https://doi.org/10.5194/acp-20-13191-2020>, 2020.
- 675
- 676 Meyer, K., Platnick, S., Oreopoulos, L., and Lee, D.: Estimating the direct radiative effect of absorbing aerosols overlying
677 marine boundary layer clouds in the southeast Atlantic using MODIS and CALIOP, *J. Geophys. Res.-Atmos.*, 118, 4801–
678 4815, <https://doi.org/10.1002/jgrd.50449>, 2013.



- 679 Mitchell, L. T., Flynn, C. J., Pistone, K., LeBlanc, S. E., Schmidt, K. S., and Redemann, J.: The complete 3-year dataset of
680 4STAR sky-scans from ORACLES 2016–2018, *Earth Syst. Sci. Data*, 17, 5303–5313, [https://doi.org/10.5194/essd-17-5303-](https://doi.org/10.5194/essd-17-5303-2025)
681 [2025](https://doi.org/10.5194/essd-17-5303-2025), 2025.
- 682
- 683 Mitchell, L. T., Flynn, C. J., Pistone, K., LeBlanc, S. E., Howell, S. G., Zuidema, P., Wood, R., and Redemann, J.: Creating
684 a comprehensive ORACLES 2016–2018 in situ SSA dataset using a refined threshold screening, *ResearchGate* [preprint],
685 <https://doi.org/10.13140/RG.2.2.17821.58086>, 16 February 2026.
- 686
- 687 Moosmüller, H., Engelbrecht, J. P., Skiba, M., Frey, G., Chakrabarty, R. K., and Arnott, W. P.: Single scattering albedo of
688 fine mineral dust aerosols controlled by iron concentration, *J. Geophys. Res.-Atmos.*, 117, D11210,
689 <https://doi.org/10.1029/2011JD016909>, 2012.
- 690
- 691 NASA GSFC: AERONET, <https://aeronet.gsfc.nasa.gov/> (last access: 10 January 2026), 2026.
- 692
- 693 NASA/LARC/SD/ASDC: ORACLES Aerosol Aircraft In Situ Data, NASA Langley Atmospheric Science Data Center
694 DAAC [data set], https://doi.org/10.5067/ASDC_DAAC/ORACLES_Aerosol_AircraftInSitu_Data_1, 2020.
- 695
- 696 Pistone, K., Redemann, J., Doherty, S., Zuidema, P., Burton, S., Cairns, B., Cochrane, S., Ferrare, R., Flynn, C., Freitag, S.,
697 Howell, S. G., Kacenelenbogen, M., LeBlanc, S., Liu, X., Schmidt, K. S., Sedlacek III, A. J., Segal-Rozenhaimer, M.,
698 Shinozuka, Y., Stammes, S., van Diedenhoven, B., Van Harten, G., and Xu, F.: Intercomparison of biomass burning aerosol
699 optical properties from in situ and remote-sensing instruments in ORACLES-2016, *Atmos. Chem. Phys.*, 19, 9181–9208,
700 <https://doi.org/10.5194/acp-19-9181-2019>, 2019.
- 701
- 702 Pistone, K., Zuidema, P., Wood, R., Diamond, M., da Silva, A. M., Ferrada, G., Saide, P. E., Ueyama, R., Ryoo, J.-M.,
703 Pfister, L., Podolske, J., Noone, D., Bennett, R., Stith, E., Carmichael, G., Redemann, J., Flynn, C., LeBlanc, S., Segal-
704 Rozenhaimer, M., and Shinozuka, Y.: Exploring the elevated water vapor signal associated with the free tropospheric
705 biomass burning plume over the southeast Atlantic Ocean, *Atmos. Chem. Phys.*, 21, 9643–9668, [https://doi.org/10.5194/acp-](https://doi.org/10.5194/acp-21-9643-2021)
706 [21-9643-2021](https://doi.org/10.5194/acp-21-9643-2021), 2021.
- 707
- 708 Pistone, K., Wilcox, E. M., Zuidema, P., Giordano, M., Podolske, J., LeBlanc, S. E., Kacenelenbogen, M., Howell, S. G.,
709 and Freitag, S.: Vertical structure of a springtime smoky and humid troposphere over the southeast Atlantic from aircraft and
710 reanalysis, *Atmos. Chem. Phys.*, 24, 7983–8005, <https://doi.org/10.5194/acp-24-7983-2024>, 2024.
- 711
- 712 Queface, A. J., Piketh, S. J., Eck, T. F., Tsay, S.-C., and Mavume, A. F.: Climatology of aerosol optical properties in
713 Southern Africa, *Atmos. Environ.*, 45, 2910–2921, <https://doi.org/10.1016/j.atmosenv.2011.01.056>, 2011.
- 714
- 715 Redemann, J., Zhang, Q., Schmid, B., Russell, P. B., Livingston, J. M., Jonsson, H., and Remer, L. A.: Assessment of
716 MODIS-derived visible and near-IR aerosol optical properties and their spatial variability in the presence of mineral dust,
717 *Geophys. Res. Lett.*, 33, L18814, <https://doi.org/10.1029/2006GL026626>, 2006.



- 718 Redemann, J., Wood, R., Zuidema, P., Doherty, S. J., Luna, B., LeBlanc, S. E., Diamond, M. S., Shinozuka, Y., Chang, I. Y.,
719 Ueyama, R., Pfister, L., Ryoo, J. M., Dobracki, A. N., da Silva, A. M., Longo, K. M., Kacenelenbogen, M. S., Flynn, C.,
720 Pistone, K., Knox, N. M., Piketh, S. J., Haywood, J., Formenti, P., Mallet, M., Stier, P., Ackerman, A. S., Bauer, S. E.,
721 Fridlind, A. M., Carmichael, G. R., Saide, P. E., Ferrada, G. A., Howell, S. G., Cairns, B., Holben, B. N., Knobelspiesse, K.
722 D., Tanelli, S., L'Ecuyer, T. S., Dzambo, A. M., Sy, O. O., McFarquhar, G. M., Poellot, M. R., Gupta, S., O'Brien, J. R.,
723 Nenes, A., Kacarab, M., Wong, J. P. S., Small-Griswold, J. D., Thornhill, K. L., Noone, D., Podolske, J. R., Schmidt, K. S.,
724 Pilewskie, P., Chen, H., Cochrane, S. P., Sedlacek, A. J., Lang, T. J., Stith, E., Segal-Rosenhaimer, M., Ferrare, R. A.,
725 Burton, S. P., Hostetler, C. A., Diner, D. J., Seidel, F. C., Platnick, S. E., Myers, J. S., Meyer, K. G., Spangenberg, D. A.,
726 Maring, H., and Gao, L.: An overview of the ORACLES (ObseRvations of Aerosols above CLouds and their intEractionS)
727 project: aerosol-cloud-radiation interactions in the southeast Atlantic basin, *Atmos. Chem. Phys.*, 21, 1507–1563,
728 <https://doi.org/10.5194/acp-21-1507-2021>, 2021.
- 729
- 730 Román, R., Benavent-Oltra, J. A., Casquero-Vera, J. A., Lopatin, A., Cazorla, A., Lyamani, H., Denjean, C., Fuertes, D.,
731 Pérez-Ramírez, D., Torres, B., Toledano, C., Dubovik, O., Cachorro, V. E., de Frutos, A. M., Olmo, F. J., and Alados-
732 Arboledas, L.: Retrieval of aerosol profiles combining sunphotometer and ceilometer measurements in GRASP code, *Atmos.*
733 *Res.*, 204, 161–177, <https://doi.org/10.1016/j.atmosres.2018.01.021>, 2018.
- 734
- 735 Russell, P. B., Bergstrom, R. W., Shinozuka, Y., Clarke, A. D., DeCarlo, P. F., Jimenez, J. L., Livingston, J. M., Redemann,
736 J., Dubovik, O., and Strawa, A.: Absorption Angstrom Exponent in AERONET and related data as an indicator of aerosol
737 composition, *Atmos. Chem. Phys.*, 10, 1155–1169, <https://doi.org/10.5194/acp-10-1155-2010>, 2010.
- 738
- 739 Ryoo, J.-M., Pfister, L., Ueyama, R., Zuidema, P., Wood, R., Chang, I., and Redemann, J.: A meteorological overview of the
740 ORACLES (ObseRvations of Aerosols above CLouds and their intEractionS) campaign over the southeastern Atlantic
741 during 2016–2018: Part 1 – Climatology, *Atmos. Chem. Phys.*, 21, 16689–16707, [https://doi.org/10.5194/acp-21-16689-](https://doi.org/10.5194/acp-21-16689-2021)
742 [2021](https://doi.org/10.5194/acp-21-16689-2021), 2021.
- 743
- 744 Sakaeda, N., Wood, R., and Rasch, P. J.: Direct and semidirect aerosol effects of southern African biomass burning aerosol,
745 *J. Geophys. Res.-Atmos.*, 116, D12, <https://doi.org/10.1029/2010JD015540>, 2011.
- 746
- 747 Schmid, B., and Wehrli, C.: Comparison of Sun photometer calibration by use of the Langley technique and the standard
748 lamp. *Appl. Optics*, 34, 4500–4512, <https://doi.org/10.1364/AO.34.004500>, 1995.
- 749
- 750 Schmidt, S. and Pilewskie, P.: Airborne measurements of spectral shortwave radiation in cloud and aerosol remote sensing
751 and energy budget studies, in: *Light Scattering Reviews*, Vol. 6, edited by: Kokhanovsky, A. A., Springer, Berlin,
752 Heidelberg, Germany, 239–288, https://doi.org/10.1007/978-3-642-15531-4_6, 2012.
- 753
- 754 Schmidt, K. S., Wendisch, M., and Kindel, B.: Airborne solar radiation sensors, in: *Springer Handbook of Atmospheric*
755 *Measurements*, edited by: Foken, T., Springer, Cham, Switzerland, 1131–1150, [https://doi.org/10.1007/978-3-030-52171-](https://doi.org/10.1007/978-3-030-52171-4_40)
756 [4_40](https://doi.org/10.1007/978-3-030-52171-4_40), 2021.
- 757
- 758 Schuster, G. L., Dubovik, O., and Holben, B. N.: Angstrom exponent and bimodal aerosol size distributions, *J. Geophys.*
759 *Res.-Atmos.*, 111, D07207, <https://doi.org/10.1029/2005JD006328>, 2006.
- 760
- 761 Sedlacek, A. J., III, Lewis, E. R., Onasch, T. B., Zuidema, P., Redemann, J., Jaffe, D., and Kleinman, L. I.: Using the Black
762 Carbon Particle Mixing State to Characterize the Lifecycle of Biomass Burning Aerosols, *Environ. Sci. Technol.*, 56, 14315–
763 14325, <https://doi.org/10.1021/acs.est.2c03851>, 2022.



- 764 Segal-Rosenheimer, M., Russell, P. B., Schmid, B., Redemann, J., Livingston, J. M., Flynn, C. J., Johnson, R. R., Dunagan,
765 S. E., Shinozuka, Y., Herman, J., Cede, A., Abuhassan, N., Comstock, J. M., Hubbe, J. M., Zelenyuk, A., and Wilson, J.:
766 Tracking elevated pollution layers with a newly developed hyperspectral sun/sky spectrometer (4STAR): Results from the
767 TCAP 2012 and 2013 campaigns. *J. Geophys. Res.-Atmos.*, 119, 5, 2611–2628, <https://doi.org/10.1002/2013JD020884>,
768 2014.
- 769
- 770 Sinyuk, A., Holben, B. N., Eck, T. F., Giles, D. M., Slutsker, I., Korkin, S., Schafer, J. S., Smirnov, A., Sorokin, M., and
771 Lyapustin, A.: The AERONET Version 3 aerosol retrieval algorithm, associated uncertainties and comparisons to Version 2,
772 *Atmos. Meas. Tech.*, 13, 3375–3411, <https://doi.org/10.5194/amt-13-3375-2020>, 2020.
- 773
- 774 Stier, P., Schutgens, N. A. J., Bellouin, N., Bian, H., Boucher, O., Chin, M., Ghan, S., Huneus, N., Kinne, S., Lin, G., Ma,
775 X., Myhre, G., Penner, J. E., Randles, C. A., Samset, B., Schulz, M., Takemura, T., Yu, F., Yu, H., and Zhou, C.: Host
776 model uncertainties in aerosol radiative forcing estimates: results from the AeroCom Prescribed intercomparison study,
777 *Atmos. Chem. Phys.*, 13, 3245–3270, <https://doi.org/10.5194/acp-13-3245-2013>, 2013.
- 778
- 779 Takemura, T., Nakajima, T., Dubovik, O., Holben, B. N., and Kinne, S.: Single-scattering albedo and radiative forcing of
780 various aerosol species with a global three-dimensional model, *J. Climate*, 15, 333–352, [https://doi.org/10.1175/1520-0442\(2002\)015<0333:SSAARF>2.0.CO;2](https://doi.org/10.1175/1520-0442(2002)015<0333:SSAARF>2.0.CO;2), 2002.
- 782
- 783 Tatro, T., and Zuidema, P.: More biomass burning aerosol is being advected westward over the southern tropical Atlantic
784 since 2003, *Sci. Total Environ.*, 965, <https://doi.org/10.1016/j.scitotenv.2025.178506>, 2025.
- 785
- 786 Taylor, J. W., Wu, H., Szpek, K., Bower, K., Crawford, I., Flynn, M. J., Williams, P. I., Dorsey, J., Langridge, J. M.,
787 Cotterell, M. I., Fox, C., Davies, N. W., Haywood, J. M., and Coe, H.: Absorption closure in highly aged biomass burning
788 smoke, *Atmos. Chem. Phys.*, 20, 11201–11221, <https://doi.org/10.5194/acp-20-11201-2020>, 2020.
- 789
- 790 van der Werf, G. R., Randerson, J. T., Giglio, L., Collatz, G. J., Mu, M., Kasibhatla, P. S., Morton, D. C., DeFries, R. S., Jin,
791 Y., and van Leeuwen, T. T.: Global fire emissions and the contribution of deforestation, savanna, forest, agricultural, and
792 peat fires (1997–2009), *Atmos. Chem. Phys.*, 10, 11707–11735, <https://doi.org/10.5194/acp-10-11707-2010>, 2010.
- 793
- 794 Virkkula, A.: Correction of the calibration of the 3-wavelength Particle Soot Absorption Photometer (3 λ PSAP), *Aerosol Sci.*
795 *Tech.*, 44, 8, 706–712, <https://doi.org/10.1080/02786826.2010.482110>, 2010.
- 796
- 797 Waquet, F., Peers, F., Ducos, F., Goloub, P., Platnick, S., Riedi, J., Tanré, D., and Thieuleux, F.: Global analysis of aerosol
798 properties above clouds, *Geophys. Res. Lett.*, 40, 5809–5814, <https://doi.org/10.1002/2013GL057482>, 2013.
- 799
- 800 Wilcox, E. M.: Direct and semi-direct radiative forcing of smoke aerosols over clouds, *Atmos. Chem. Phys.*, 12, 139–149,
801 <https://doi.org/10.5194/acp-12-139-2012>, 2012.
- 802
- 803 Wu, H., Taylor, J. W., Szpek, K., Langridge, J. M., Williams, P. I., Flynn, M., Allan, J. D., Abel, S. J., Pitt, J., Cotterell, M.
804 I., Fox, C., Davies, N. W., Haywood, J., and Coe, H.: Vertical variability of the properties of highly aged biomass burning
805 aerosol transported over the southeast Atlantic during CLARIFY-2017, *Atmos. Chem. Phys.*, 20, 12697–12719,
806 <https://doi.org/10.5194/acp-20-12697-2020>, 2020.
- 807
- 808 Zhang, A., Wang, Y., Zhang, Y., Weber, R. J., Song, Y., Ke, Z., and Zou, Y.: Modeling the global radiative effect of brown
809 carbon: a potentially larger heating source in the tropical free troposphere than black carbon, *Atmos. Chem. Phys.*, 20, 1901–
810 1920, <https://doi.org/10.5194/acp-20-1901-2020>, 2020.



- 811 Zuidema, P., Redemann, J., Haywood, J., Wood, R., Piketh, S. J., Hipondoka, M., and Formenti, P.: Smoke and Clouds
812 above the Southeast Atlantic: Upcoming Field Campaigns Probe Absorbing Aerosol's Impact on Climate, *B. Am. Meteorol.*
813 *Soc.*, 97, 1131–1135, <https://doi.org/10.1175/BAMS-D-15-00082.1>, 2016.
814
815 Zuidema, P., Sedlacek III, A. J., Flynn, C., Springston, S., Delgadillo, R., Zhang, J., Aiken, A. C., Koontz, A., and
816 Muradyan, P.: The Ascension Island boundary layer in the remote Southeast Atlantic is often smoky, *Geophys. Res. Lett.*,
817 45, 4456–4465, <https://doi.org/10.1002/2017GL076926>, 2018.